Engineering Analysis with Boundary Elements 158 (2024) 239–251

Contents lists available at ScienceDirect

Engineering Analysis with Boundary Elements

journal homepage: www.elsevier.com/locate/enganabound

Boundary integral formulation of the cell-by-cell model of cardiac electrophysiology☆

Giacomo Rosilho de Souza [a], Rolf Krause [a,b], Simone Pezzuto [c,a,*]

[a] Center for Computational Medicine in Cardiology, Euler Institute, Università della Svizzera italiana, via G. Buffi 13, 6900, Lugano, Switzerland
[b] Faculty of Mathematics and Informatics, FernUni, Schinerstrasse 18, 3900, Brig, Switzerland
[c] Laboratory of Mathematics for Biology And Medicine, Department of Mathematics, University of Trento, via Sommarive 14, 38123, Trento, Italy

ARTICLE INFO

Dataset link: .

Keywords:
Cell-by-cell model
EMI model
Boundary element method
Cardiac electrophysiology
Gap junctions

ABSTRACT

We propose a boundary element method for the accurate solution of the cell-by-cell bidomain model of electrophysiology. The cell-by-cell model, also called Extracellular-Membrane-Intracellular (EMI) model, is a system of reaction–diffusion equations describing the evolution of the electric potential within each domain: intra- and extra-cellular space and the cellular membrane. The system is parabolic but degenerate because the time derivative is only in the membrane domain. In this work, we adopt a boundary-integral formulation for removing the degeneracy in the system and recast it to a parabolic equation on the membrane. The formulation is also numerically advantageous since the number of degrees of freedom is sensibly reduced compared to the original model. Specifically, we prove that the boundary-element discretization of the EMI model is equivalent to a system of ordinary differential equations, and we consider a time discretization based on the multirate explicit stabilized Runge–Kutta method. We numerically show that our scheme convergences exponentially in space for the single-cell case. We finally provide several numerical experiments of biological interest.

1. Introduction

The human heart is composed of billions of electrically-active myocytes. Altogether, myocytes form a syncytium of cells that enables electrical and mechanical synchronization of the tissue [1]. Cardiac myocytes are excitable cells that can react and transmit electric currents to communicate and coordinate their action. Electrical propagation depends on the conductive properties of the cytoplasm and the extracellular matrix. Cell-to-cell conduction occurs via gap junctions, permeable channels mostly distributed in the myocyte longitudinal direction. Myocyte excitability is due to hundreds of thousands ion channels embedded in the cellular membrane. The overall propagation of the cardiac action potential emerges from a balance of diffusion and transmembrane currents.

Mathematically, cardiac electrophysiology models are systems of reaction–diffusion equations. The reaction term results from transmembrane currents, which are voltage-dependent and regulated through a gating mechanism. Ion channel gating is typically modeled via Hodgkin–Huxley formalism, yielding a possibly large set of ordinary differential equations. The diffusion term captures the spatial coordination of the cardiac tissue. The state-of-the-art model is the bidomain system. Here, the intracellular and extracellular spaces are superimposed and homogenized [2]. Patient-specific organ-scale simulations routinely employ the bidomain model and its monodomain approximation. Despite being physiologically accurate, the bidomain model fails to capture the sub-cellular tissue organization. The cell-by-cell bidomain model accounts for the Extracellular-Membrane-Intracellular (EMI) tissue components as separated (yet coupled) entities [3,4]. The cell-by-cell model enables a more accurate description of tissue heterogeneities, a key aspect in heart failure and atrial fibrillation [5].

The cell-by-cell model presents several challenges. First, it has an unusual mathematical formulation showing time dynamics at the boundaries, indeed it presents an ordinary differential equation (ODE) on the transmembrane boundary and a constraint on the gap junctions. Second, in addition to the natural stiffness introduced by the Laplacian, the ionic model introduces stiff nonlinear multiscale dynamics. Third, a full scale heart model would require billions of cells leading to an incredibly large system of equations. Hence, advanced tailored methods must be designed to solve cell-by-cell models.

In the literature, cell-by-cell models have already been solved by means of the finite element or boundary element method. In the finite

☆ This work was supported by the European High-Performance Computing Joint Undertaking EuroHPC under grant agreement No 955495 (MICROCARD) co-funded by the Horizon 2020 programme of the European Union (EU) and the Swiss State Secretariat for Education, Research and Innovation.

* Corresponding author at: Laboratory of Mathematics for Biology And Medicine, Department of Mathematics, University of Trento, via Sommarive 14, 38123, Trento, Italy.

E-mail addresses: giacomo.rosilhodesouza@usi.ch (G. Rosilho de Souza), rolf.krause@usi.ch (R. Krause), simone.pezzuto@unitn.it (S. Pezzuto).

https://doi.org/10.1016/j.enganabound.2023.10.021
Received 10 February 2023; Received in revised form 3 October 2023; Accepted 17 October 2023
Available online 3 November 2023

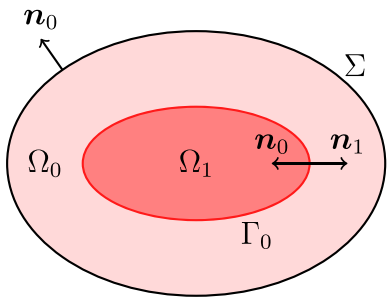

Fig. 1. Geometrical setup of problem Eq. (1). The cell and the extra-cellular space are respectively denoted by Ω_1 and Ω_0. The cellular membrane is Γ_0.

element community the problem has been tackled by Stinstra and collaborators [6–9] and more recently by Tveito and collaborators [4,10–12] as well. In both cases the cell-by-cell model was employed to study the effects of the cells microscopic structure on macroscopic values as conductive velocity or effective tissue conductivity. Also, the cell-by-cell model was employed to derive the effective parameters for the bidomain model under different microstructural conditions [3,7,13]. Bécue, Potse and Coudière [14–16] compared different gap junctions modelizations and studied existence of solutions in [17]. In the context of the boundary element method the model was solved only for very simple and structured geometries, for instance in [18–20] for a longitudinal array of non-touching cells, in [21] for a two-cells model, and more recently, from a theoretical point of view, in [22,23] it was analyzed for the case of isolated cells.

In this paper we propose a spatial discretization of the cell-by-cell model based on the boundary element method (BEM) and reduce it to a single system of ODEs living only on the transmembrane boundary. The great advantage brought by the BEM is that only boundaries need to be discretized, leading to much smaller systems of equations compared to more traditional methods as finite elements or volumes. We stress that the approach presented here is easily adapted for different gap-junction boundary conditions [4] or unbounded extracellular domains (the "infinite bath" approximation). Also, any spatial discretization method for which Dirichlet-to-Neumann maps can be computed could be employed instead of the BEM. Compared to previous BEM approaches, our methodology is independent from the cells structure and reduces any problem to an ODE on the transmembrane boundary.

This paper is organized as follows. In Section 2 we treat the simple case where only one myocyte cell is present, the purpose of this section is to introduce the needed tools and our approach in a simplified setting. In Section 3 instead we discretize in space the full problem with an arbitrary number of cells, possibly in contact, and reduce it to a system of ODEs. Finally, in Section 4 we present some numerical results.

2. The single-cell problem

The main purpose of this section is to introduce in a simplified setting the boundary integral formulation and the boundary element method (BEM) employed to discretize the full problem, done in Section 3, and as well the approach used to reduce the space discrete problem into a system of ordinary differential equations (ODE).

2.1. Problem formulation

Here we consider the EMI model for a single cell, denoted by the bounded domain $\Omega_1 \subset \mathbb{R}^d$ with $d = 2$, embedded in the extracellular space, denoted by $\Omega_0 \subset \mathbb{R}^d$. See Fig. 1 for a schematic representation of the single-cell problem. Specifically, we require that the intra- and extra-cellular domain do not overlap, that is $\Omega_0 \cap \Omega_1 = \emptyset$, and that they share a common boundary $\Gamma_0 = \bar{\Omega}_0 \cap \bar{\Omega}_1$. The boundary Γ_0 represents the cellular membrane. The membrane model and temporal dynamic of the system, due to capacitative currents, is confined on Γ_0. We finally assume that Ω_0 is bounded with exterior boundary $\Sigma = \partial\Omega_0 \setminus \Gamma_0$. Also, we define $\Gamma_1 = \partial\Omega_1$ (note that for the single-cell problem $\Gamma_1 = \Gamma_0$). The single-cell problem reads as follows:

$$
\begin{cases}
-\sigma_1 \Delta u_1(\boldsymbol{x},t) = 0, & \text{in } \Omega_1, \quad \text{(a)}\\
-\sigma_0 \Delta u_0(\boldsymbol{x},t) = 0, & \text{in } \Omega_0, \quad \text{(b)}\\
\sigma_1 \partial_{\boldsymbol{n}_1} u_1(\boldsymbol{x},t) + \sigma_0 \partial_{\boldsymbol{n}_0} u_0(x,t) = 0, & \text{on } \Gamma_0, \quad \text{(c)}\\
\sigma_0 \partial_{\boldsymbol{n}_0} u_0(\boldsymbol{x},t) = I_{\mathrm{t}}(\boldsymbol{x},t), & \text{on } \Gamma_0, \quad \text{(d)}\\
C_{\mathrm{m}} \partial_t V_0(\boldsymbol{x},t) + I_{\mathrm{ion}}\big(V_0(\boldsymbol{x},t), z(\boldsymbol{x},t)\big) = I_{\mathrm{t}}(\boldsymbol{x},t), & \text{on } \Gamma_0, \quad \text{(e)}\\
u_1(\boldsymbol{x},t) - u_0(\boldsymbol{x},t) = V_0(\boldsymbol{x},t), & \text{on } \Gamma_0, \quad \text{(f)}\\
\partial_t z(\boldsymbol{x},t) = g\big(V_0(\boldsymbol{x},t), z(\boldsymbol{x},t)\big), & \text{on } \Gamma_0, \quad \text{(g)}\\
\sigma_0 \partial_{\boldsymbol{n}_0} u_0(\boldsymbol{x},t) = 0, & \text{on } \Sigma, \quad \text{(h)}\\
u_0(\boldsymbol{x},0) = u_0^0(\boldsymbol{x}), & \text{on } \Gamma_0, \quad \text{(i)}\\
u_1(\boldsymbol{x},0) = u_1^0(\boldsymbol{x}), & \text{on } \Gamma_0, \quad \text{(j)}
\end{cases}
\tag{1}
$$

where the unknowns $u_0(\boldsymbol{x},t)$, $u_1(\boldsymbol{x},t)$, $V_0(\boldsymbol{x},t)$ and $z(\boldsymbol{x},t)$ are respectively the intra-cellular, extra-cellular, transmembrane electric potential, and a vector of gating and concentration variables. The auxiliary current $I_{\mathrm{t}}(\boldsymbol{x},t)$ is defined in Eq. (1)(e) and is employed to alleviate the notation only. Coefficients $\sigma_0 > 0$ and $\sigma_1 > 0$ are respectively the extra- and intra-cellular electric conductivity, $C_{\mathrm{m}} > 0$ is the membrane capacitance, and $\boldsymbol{n}_i$, $i = 0, 1$ is the outwards normal to $\partial\Omega_i$. The ionic model is typically based on the Hodgkin–Huxley formalism, where $I_{\mathrm{ion}}(V_0, z)$ is a sum of ionic currents and the system of ODEs in Eq. (1)(g) describes the gating dynamic. Note that the initial datum is of degenerate type, as we assign $u_0^0(\boldsymbol{x})$ and $u_1^0(\boldsymbol{x})$ only on Γ_0, consistently with the differential–algebraic structure of the model [24].

The global well-posedness of the three-dimensional version of problem (1) in Sobolev spaces has been studied by Matano and Mori [25]. The idea of the proof is similar to what we do here, in the sense that the authors recast (1) to an ODE on the interface Γ_0. The equation involves a pseudo-differential operator not dissimilar to the Dirichlet-Neumann map, as done below in the discrete settings with the operator ψ. For (1), the solution is defined up to a constant, which is typically fixed by imposing an extra condition on the extracellular potential, e.g., its average value on the outer boundary. This is done also in the standard bidomain model [26]. In [25], the authors consider Ω_1 with a smooth boundary Γ_0 and unbounded $\Omega_0 = \mathbb{R}^3 \setminus (\Omega_1 \cup \Gamma_0)$. Coefficients C_m, σ_0, and σ_1 are positive scalars and, due to unboundedness of Ω_0, Eq. (1)(h) is replaced with a vanishing condition $u_0(\boldsymbol{x}) \to 0$ as $\|\boldsymbol{x}\| \to \infty$. With continuous initial values on Γ_0, and I_{ion}, g smooth functions, the local existence and uniqueness of a solution can be proved. They also prove global existence of solutions for the particular case of the FitzHugh–Nagumo and Hodgkin–Huxley ionic models. The well-posedness of the multi-cell problem has been analyzed by Colli Franzone and Savaré [24].

2.2. Boundary integral formulation

Problem in Eq. (1) has already been tackled and carefully analyzed by Henríquez et al. [23], where the BEM with a Galerkin approach was employed. Here, we derive a boundary integral formulation of the unicellular problem Eq. (1) in terms of trace operators and Poincaré–Steklov operators. For the sake of simplicity, we henceforth drop the explicit dependency on $(\boldsymbol{x}, t)$, unless differently stated.

Let γ_t^1 be the trace operator and γ_n^1 the conormal derivative on the boundary Γ_1. More specifically, we introduce the operators as follows:

$$
\begin{aligned}
&\gamma_t^1 : H^1(\Omega_1) \to H^{1/2}(\Gamma_1), \qquad \gamma_t^1 u_1(\boldsymbol{x}) = \lim_{\Omega_1 \ni \boldsymbol{y} \to \boldsymbol{x} \in \Gamma_1} u_1(\boldsymbol{y}),\\
&\gamma_n^1 : H^1(\Omega_1) \to H^{-1/2}(\Gamma_1), \qquad \gamma_n^1 u_1(\boldsymbol{x}) = \lim_{\Omega_1 \ni \boldsymbol{y} \to \boldsymbol{x} \in \Gamma_1} \langle \nabla u_1(\boldsymbol{y}), \boldsymbol{n}_1 \rangle,
\end{aligned}
\tag{2}
$$

where the limits on the right must hold for smooth enough u_1. Let $G(\boldsymbol{x},\boldsymbol{y})$ be the fundamental solution of the Laplacian in $\mathbb{R}^d$, the Green representation formula for u_1 satisfying Eq. (1)(a) implies that

$$u_1(\boldsymbol{x}) = \int_{\Gamma_1} \gamma^1_{t,\boldsymbol{y}} G(\boldsymbol{x},\boldsymbol{y})\gamma^1_n u_1(\boldsymbol{y})\mathrm{d}s_{\boldsymbol{y}} - \int_{\Gamma_1} \gamma^1_{n,\boldsymbol{y}} G(\boldsymbol{x},\boldsymbol{y})\gamma^1_t u_1(\boldsymbol{y})\mathrm{d}s_{\boldsymbol{y}}, \quad \boldsymbol{x}\in\Omega_1 \tag{3}$$

where $\boldsymbol{y}$ in $\gamma^1_{t,\boldsymbol{y}}, \gamma^1_{n,\boldsymbol{y}}$ means that the operators are applied to the second variable of $G(\boldsymbol{x},\boldsymbol{y})$. Taking the trace γ^1_t of Eq. (3) we obtain

$$\gamma^1_t u_1 = \mathcal{V}_1\gamma^1_n u_1 - (\mathcal{K}_1 - \tfrac{1}{2}I)\gamma^1_t u_1, \tag{4}$$

where I is the identity operator, $\mathcal{V}_1$ and $\mathcal{K}_1$ are the single and double layer operators defined by

$$\begin{aligned} &\mathcal{V}_1 : H^{-1/2}(\Gamma_1)\to H^{1/2}(\Gamma_1), \qquad \mathcal{V}_1\rho(\boldsymbol{x}) = \int_{\Gamma_1}\gamma^1_{t,\boldsymbol{y}}G(\boldsymbol{x},\boldsymbol{y})\rho(\boldsymbol{y})\mathrm{d}s_{\boldsymbol{y}}, \qquad \boldsymbol{x}\in\Gamma_1,\\ &\mathcal{K}_1 : H^{1/2}(\Gamma_1)\to H^{1/2}(\Gamma_1), \qquad \mathcal{K}_1\rho(\boldsymbol{x}) = \int_{\Gamma_1}\gamma^1_{n,\boldsymbol{y}}G(\boldsymbol{x},\boldsymbol{y})\rho(\boldsymbol{y})\mathrm{d}s_{\boldsymbol{y}}, \qquad \boldsymbol{x}\in\Gamma_1, \end{aligned} \tag{5}$$

and the term $\frac{1}{2}I$ in Eq. (4) comes from the jump of the double layer potential as $\Omega_1 \ni \boldsymbol{x}\to\boldsymbol{y}\in\Gamma_1$. Problem Eq. (4) can be rewritten as

$$\mathcal{V}_1\gamma^1_n u_1 = (\mathcal{K}_1 + \tfrac{1}{2}I)\gamma^1_t u_1, \tag{6}$$

or employing the Poincaré–Steklov operator (Dirichlet-to-Neumann map):

$$\mathcal{P}_1 : H^{1/2}(\Gamma_1)\to H^{-1/2}(\Gamma_1), \qquad \mathcal{P}_1 := \mathcal{V}_1^{-1}(\mathcal{K}_1 + \tfrac{1}{2}I), \tag{7}$$

then Eq. (6) becomes

$$\gamma^1_n u_1 = \mathcal{P}_1\gamma^1_t u_1. \tag{8}$$

The invertibility of $\mathcal{V}_1$ is ensured under the condition $\mathrm{diam}(\Omega_1) < 1$, which is always satisfied under a suitable scaling. The Poincaré–Steklov operator $\mathcal{P}_1$ in Eq. (7) is known to be symmetric [27, Section 3.7]. Now, let $\gamma^0_t u_0$, $\gamma^0_n u_0$ be the trace and conormal derivative of u_0 on $\Gamma_0 = \Gamma_1$, respectively. In order to derive a Dirichlet-to-Neumann map $\mathcal{P}_0 : H^{1/2}(\Gamma_0)\to H^{-1/2}(\Gamma_0)$ in Ω_0, hence

$$\gamma^0_n u_0 = \mathcal{P}_0\gamma^0_t u_0, \tag{9}$$

we need to take into account the boundary condition (1)(h) on the external boundary Σ of Ω_0. In order to alleviate the presentation we postpone the derivation of $\mathcal{P}_0$ to Appendix. However, we would like to note that $\mathcal{P}_0$ remains symmetric.

Due to the Green representation formula, Eqs. (1)(a) and (1)(b) can be dropped from Eq. (1). Also, Eq. (1)(h) is encoded into the definition of $\mathcal{P}_0$ (see Appendix). Finally, the boundary integral formulation of Eq. (1) is

$$\begin{cases} \sigma_1\mathcal{P}_1\gamma^1_t u_1 + \sigma_0\mathcal{P}_0\gamma^0_t u_0 = 0, & \text{(a)}\\ \gamma^1_t u_1 - \gamma^0_t u_0 = V_0, & \text{(b)}\\ \sigma_0\mathcal{P}_0\gamma^0_t u_0 = I_{\mathrm{t}}(V_0, z), & \text{(c)}\\ \partial_t z = g(V_0, z). & \text{(d)} \end{cases} \tag{10}$$

2.3. Spatial discretization of the unicellular problem

We adopt the collocation BEM as spatial discretization scheme. Boundary element methods have less degrees of freedom than other standard techniques, while the collocation approach yields lower dimensional boundary integrals than the variational method and hence faster computations. For extensive presentations on the BEM we refer to [27–29].

We place M collocation points $\boldsymbol{x}_j$, $j = 1,\dots,M$, on Γ_1 in a counterclockwise order. Then we compute a smooth parametrization $\gamma_{\Gamma_1} : [0,1)\to\Gamma_1$ satisfying

$$\gamma_{\Gamma_1}(t_j) = \boldsymbol{x}_j \quad j = 1,\dots,M, \tag{11}$$

where $\{t_j\}_{j=1}^M \subset [0,1)$ is an increasing sequence. (The parametrization γ_{Γ_1} is computed with Fourier interpolation. For the unicellular problem, we could define $\gamma_{\Gamma_1}(t)$ first and then set $\boldsymbol{x}_j$ as in Eq. (11). However, this is not possible for the multi-cell problems.) Finally, we represent $\gamma^1_t u_1$, $\gamma^1_n u_1$ as

$$\gamma^1_t u_1(\gamma_{\Gamma_1}(t)) = \sum_{j=1}^M u_1^j L_j(t), \quad \gamma^1_n u_1(\gamma_{\Gamma_1}(t)) = \sum_{j=1}^M \tilde{u}_1^j L_j(t), \tag{12}$$

where $L_j(t)$ are trigonometric Lagrange polynomials satisfying $L_j(t_k) = \delta_{jk}$ for $j,k = 1,\dots,M$. Instead of Eq. (6) we solve the weaker form

$$\mathcal{V}_1\gamma^1_n u_1(\boldsymbol{x}_k) = (\mathcal{K}_1 + \tfrac{1}{2}I)\gamma^1_t u_1(\boldsymbol{x}_k), \qquad k = 1,\dots,M, \tag{13}$$

with $\boldsymbol{x}_k = \gamma_{\Gamma_1}(t_k)$, which is equivalent to

$$\sum_{j=1}^M \tilde{u}_1^j \mathcal{V}_1 L_j(\gamma^{-1}_{\Gamma_1}(\boldsymbol{x}_k)) = \sum_{j=1}^M u_1^j(\mathcal{K}_1 + \tfrac{1}{2}I)L_j(\gamma^{-1}_{\Gamma_1}(\boldsymbol{x}_k)), \qquad k = 1,\dots,M, \tag{14}$$

and hence the linear system

$$V_1\tilde{\boldsymbol{u}}_1 = (K_1 + \tfrac{1}{2}I)\boldsymbol{u}_1, \tag{15}$$

with $\boldsymbol{u}_1, \tilde{\boldsymbol{u}}_1$ the vectors of coefficients $u_1^j, \tilde{u}_1^j$, respectively, and

$$\begin{aligned} (V_1)_{kj} &:= \mathcal{V}_1(L_j\circ\gamma^{-1}_{\Gamma_1})(\boldsymbol{x}_k) = \int_{\Gamma_1}\gamma^1_{t,\boldsymbol{y}}G(\boldsymbol{x}_k,\boldsymbol{y})L_j(\gamma^{-1}_{\Gamma_1}(\boldsymbol{y}))\mathrm{d}s_{\boldsymbol{y}}\\ &= \int_0^1 \gamma^1_{t,\boldsymbol{y}}G(\boldsymbol{x}_k,\gamma_{\Gamma_1}(t))L_j(t)\|\gamma'_{\Gamma_1}(t)\|\mathrm{d}t,\\ (K_1)_{kj} &:= \mathcal{K}_1(L_j\circ\gamma^{-1}_{\Gamma_1})(\boldsymbol{x}_k) = \int_{\Gamma_1}\gamma^1_{n,\boldsymbol{y}}G(\boldsymbol{x}_k,\boldsymbol{y})L_j(\gamma^{-1}_{\Gamma_1}(\boldsymbol{y}))\mathrm{d}s_{\boldsymbol{y}}\\ &= \int_0^1 \gamma^1_{n,\boldsymbol{y}}G(\boldsymbol{x}_k,\gamma_{\Gamma_1}(t))L_j(t)\|\gamma'_{\Gamma_1}(t)\|\mathrm{d}t. \end{aligned}$$

The matrix coefficients $(V_1)_{kj}$, $(K_1)_{kj}$ must be computed with special care due to the singularities in the fundamental solution $G(\boldsymbol{x},\boldsymbol{y})$ and its derivatives as $\gamma_{\Gamma_1}(t)\to\boldsymbol{x}_k$, we refer to [28,30] for the details.

Note that $\boldsymbol{u}_1$ and $\tilde{\boldsymbol{u}}_1$ are the vectors of coordinates of $\gamma^1_t u_1$ and $\gamma^1_n u_1$, respectively, and that from Eq. (15) follows the discrete version of Eq. (8)

$$\tilde{\boldsymbol{u}}_1 = P_1\boldsymbol{u}_1, \quad P_1 := (V_1)^{-1}(K_1 + \tfrac{1}{2}I), \tag{16}$$

where P_1 is the discrete Poincaré–Steklov operator (Dirichlet-to-Neumann map) in Ω_1. Similarly, in Appendix we derive the discrete version of Eq. (9) and obtain

$$\tilde{\boldsymbol{u}}_0 = P_0\boldsymbol{u}_0, \tag{17}$$

with $\boldsymbol{u}_0$ and $\tilde{\boldsymbol{u}}_0$ the vectors of coordinates of $\gamma^0_t u_0$ and $\gamma^0_n u_0$, respectively.

Finally, the space discretization of the boundary integral formulation Eq. (10) is

$$\begin{cases} \sigma_1 P_1\boldsymbol{u}_1 + \sigma_0 P_0\boldsymbol{u}_0 = 0, & \text{(a)}\\ \boldsymbol{u}_1 - \boldsymbol{u}_0 = \boldsymbol{V}_0, & \text{(b)}\\ \sigma_0 P_0\boldsymbol{u}_0 = I_{\mathrm{t}}(\boldsymbol{V}_0, \boldsymbol{z}), & \text{(c)}\\ \boldsymbol{z}' = g(\boldsymbol{V}_0, \boldsymbol{z}), & \text{(d)} \end{cases} \tag{18}$$

where $\boldsymbol{V}_0(t)\in\mathbb{R}^M$ is the vector whose coefficients represent $V_0(\boldsymbol{x}_j, t)$ and analogously for $\boldsymbol{z}$. The right-hand sides I_{t} and g are applied to $\boldsymbol{V}_0, \boldsymbol{z}$ component wise. If needed, the solution u_1 satisfying Eq. (1)(a) is approximated via the Green identity Eqs. (3) and (12), (16). We proceed similarly for u_0.

2.4. The Lagrange multipliers approach for the unicellular problem

Now we solve Eq. (18) and to do so we employ the Lagrange multiplier method. We adopted this technique mainly for pedagogical reasons in regard of what will be presented in Section 3, since for the unicellular problem Eq. (1) a more direct approach could be used.

In the remaining of this section we construct the linear map

$$\psi : \mathbb{R}^M \to \mathbb{R}^M, \qquad \psi(\boldsymbol{V}_0) = \sigma_0 P_0 \boldsymbol{u}_0, \tag{19}$$

where $\boldsymbol{u}_0$ satisfies Eqs. (18)(a) and (18)(b) (behind the scenes $\boldsymbol{u}_1$ is computed as well, but it is not needed as output of ψ). Inserting Eq. (19) and $I_{\mathrm{t}}(\boldsymbol{V}_0, \boldsymbol{z}) = C_{\mathrm{m}}\boldsymbol{V}_0' + I_{\mathrm{ion}}(\boldsymbol{V}_0, \boldsymbol{z})$ in Eqs. (18)(c) and (18)(d) the problem reduces to the ODE

$$\begin{cases} C_{\mathrm{m}}\boldsymbol{V}_0' + I_{\mathrm{ion}}(\boldsymbol{V}_0, \boldsymbol{z}) = \psi(\boldsymbol{V}_0), & \text{(a)} \\ \boldsymbol{z}' = g(\boldsymbol{V}_0, \boldsymbol{z}), & \text{(b)} \end{cases} \tag{20}$$

which can be integrated by any suitable time marching scheme. Eq. (20) has the same structure as the one derived in [23], where a BEM for the cell-by-cell model without gap junctions is derived.

Theorem 2.1 is the unicellular version of the more general Theorem 3.1 below, which in turn takes inspiration from the work in [31]. We also remark that the Theorem is independent of the spatial discretization. For instance, a finite element discretization may be recast to Eq. (18) by static condensation, that is by explicitly computing the discrete Poincaré–Steklov operator.

Theorem 2.1. *The linear map ψ from Eq. (19) satisfies $\psi(\boldsymbol{V}_0) = \lambda$, with $\lambda \in \mathbb{R}^M$ and $\beta_1 \in \mathbb{R}$ solution to*

$$\begin{pmatrix} F & G \\ G^\top & 0 \end{pmatrix} \begin{pmatrix} \lambda \\ \beta_1 \end{pmatrix} = \begin{pmatrix} \boldsymbol{V}_0 \\ 0 \end{pmatrix}. \tag{21}$$

The matrices $F \in \mathbb{R}^{M\times M}$, $G \in \mathbb{R}^M$ are defined by

$$F = -(\sigma_1^{-1}(P_1^+)^{-1} + \sigma_0^{-1}(P_0^+)^{-1}), \qquad G = \boldsymbol{e}, \tag{22}$$

$\boldsymbol{e} \in \mathbb{R}^M$ is the vector of ones and

$$P_0^+ = P_0 + \alpha_0 \boldsymbol{e}\boldsymbol{e}^\top, \qquad P_1^+ = P_1 + \alpha_1 \boldsymbol{e}\boldsymbol{e}^\top, \tag{23}$$

with $\alpha_0, \alpha_1 > 0$. If needed, a solution $\boldsymbol{u}_0, \boldsymbol{u}_1$ to Eqs. (18)(a) and (18)(b) is computed with

$$\boldsymbol{u}_0 = \sigma_0^{-1}(P_0^+)^{-1}\lambda, \qquad \boldsymbol{u}_1 = -\sigma_1^{-1}(P_1^+)^{-1}\lambda + \beta_1 \boldsymbol{e}. \tag{24}$$

All unknowns $\lambda, \beta_1, \boldsymbol{u}_0, \boldsymbol{u}_1$ are independent from $\alpha_0, \alpha_1 > 0$.

Hence, when solving the ODE system Eq. (20) with a time integration scheme, every time that $\psi(\boldsymbol{V}_0)$ needs to be evaluated system Eq. (21) is solved and $\psi(\boldsymbol{V}_0) = \lambda$ is inserted in Eq. (20).

Before proving Theorem 2.1, we show the following results on the pseudoinverses P_0^+, P_1^+ of P_0, P_1, respectively.

Lemma 2.2. *Let $P = P_0$ or $P = P_1$ and $P^+ = P + \alpha \boldsymbol{e}\boldsymbol{e}^\top$ for $\alpha > 0$. Let $\lambda \in \mathbb{R}^M$ such that $\langle \lambda, \boldsymbol{e}\rangle = 0$, then*

$$\langle (P^+)^{-1}\lambda, \boldsymbol{e}\rangle = 0. \tag{25}$$

Moreover, for $\beta \in \mathbb{R}$, $\sigma \in \mathbb{R}^*$ and

$$\boldsymbol{u} = \sigma^{-1}(P^+)^{-1}\lambda + \beta \boldsymbol{e} \tag{26}$$

it holds $\langle \boldsymbol{u}, \boldsymbol{e}\rangle = \beta M$, $\sigma P \boldsymbol{u} = \lambda$ and $\boldsymbol{u}$ is independent from α.

Proof. Since P is positive semi-definite, with $P\boldsymbol{e} = 0$, then P^+ is positive definite. Let $\boldsymbol{x} = (P^+)^{-1}\lambda$, then

$$\alpha\langle \boldsymbol{e}, \boldsymbol{e}\rangle\langle \boldsymbol{x}, \boldsymbol{e}\rangle = \langle \alpha \boldsymbol{e}\boldsymbol{e}^\top \boldsymbol{x}, \boldsymbol{e}\rangle = \langle (P + \alpha \boldsymbol{e}\boldsymbol{e}^\top)\boldsymbol{x}, \boldsymbol{e}\rangle = \langle P^+\boldsymbol{x}, \boldsymbol{e}\rangle = \langle \lambda, \boldsymbol{e}\rangle = 0 \tag{27}$$

and thus $\langle \boldsymbol{x}, \boldsymbol{e}\rangle = 0$, which proves Eq. (25). From Eqs. (26) and (25), we have

$$\langle \boldsymbol{u}, \boldsymbol{e}\rangle = \beta\langle \boldsymbol{e}, \boldsymbol{e}\rangle = \beta M. \tag{28}$$

Now we are in position to show that $\sigma P \boldsymbol{u} = \lambda$, which follows from

$$\sigma(P + \alpha \boldsymbol{e}\boldsymbol{e}^\top)\boldsymbol{u} = \lambda + \beta\sigma(P + \alpha \boldsymbol{e}\boldsymbol{e}^\top)\boldsymbol{e} \tag{29}$$

and

$$\sigma\alpha \boldsymbol{e}\boldsymbol{e}^\top \boldsymbol{u} = \sigma\alpha\beta \boldsymbol{e} M = \sigma\alpha\beta \boldsymbol{e}\boldsymbol{e}^\top \boldsymbol{e}. \tag{30}$$

It remains to show that $\boldsymbol{u}$ is independent from α. To do so, we show that $(P^+)^{-1}\lambda = (\tilde{P}^+)^{-1}\lambda$, with $\tilde{P}^+ = P + \tilde{\alpha}\boldsymbol{e}\boldsymbol{e}^\top$, $\tilde{\alpha} > 0$. We compute

$$\begin{aligned} \tilde{P}^+((\tilde{P}^+)^{-1}\lambda - (P^+)^{-1}\lambda) &= \lambda - \tilde{P}^+(P^+)^{-1}\lambda \\ &= \lambda - (P^+ + (\tilde{\alpha} - \alpha)\boldsymbol{e}\boldsymbol{e}^\top)(P^+)^{-1}\lambda \\ &= (\alpha - \tilde{\alpha})\boldsymbol{e}\boldsymbol{e}^\top(P^+)^{-1}\lambda = 0. \end{aligned} \tag{31}$$

The last equality follows from Eq. (25), and $(P^+)^{-1}\lambda = (\tilde{P}^+)^{-1}\lambda$ from invertibility of $\tilde{P}^+$. □

Proof of Theorem 2.1. Note that if vectors $\boldsymbol{u}_0, \boldsymbol{u}_1$ are solutions to Eqs. (18)(a) and (18)(b), then also $\boldsymbol{u}_0 + C\boldsymbol{e}$, $\boldsymbol{u}_1 + C\boldsymbol{e}$ are solutions for all $C \in \mathbb{R}$; indeed, $P_0\boldsymbol{e} = P_1\boldsymbol{e} = \boldsymbol{0}$. Hence, in what follows, we choose to fix such free constant by imposing $\langle \boldsymbol{u}_0, \boldsymbol{e}\rangle = 0$.

Since P_0, P_1 are symmetric, $\boldsymbol{u}_0$, $\boldsymbol{u}_1$, are also solution to the constrained minimization problem

$$\min_{\boldsymbol{u}_1, \boldsymbol{u}_0} \frac{\sigma_0}{2}\langle P_0\boldsymbol{u}_0, \boldsymbol{u}_0\rangle + \frac{\sigma_1}{2}\langle P_1\boldsymbol{u}_1, \boldsymbol{u}_1\rangle \quad \text{with} \quad \boldsymbol{u}_1 - \boldsymbol{u}_0 = \boldsymbol{V}_0, \quad \langle \boldsymbol{u}_0, \boldsymbol{e}\rangle = 0. \tag{32}$$

Let

$$\mathcal{L}(\boldsymbol{u}_0, \boldsymbol{u}_1, \lambda, \mu) = \frac{\sigma_0}{2}\langle P_0\boldsymbol{u}_0, \boldsymbol{u}_0\rangle + \frac{\sigma_1}{2}\langle P_1\boldsymbol{u}_1, \boldsymbol{u}_1\rangle + \langle \boldsymbol{u}_1 - \boldsymbol{u}_0 - \boldsymbol{V}_0, \lambda\rangle + \langle \boldsymbol{u}_0, \boldsymbol{e}\rangle\mu \tag{33}$$

be the Lagrangian function, imposing $\nabla\mathcal{L}(\boldsymbol{u}_0, \boldsymbol{u}_1, \lambda, \mu) = \boldsymbol{0}$ yields

$$\sigma_0 P_0\boldsymbol{u}_0 - \lambda + \boldsymbol{e}\mu = \boldsymbol{0}, \qquad \sigma_1 P_1\boldsymbol{u}_1 + \lambda = \boldsymbol{0}, \tag{34}$$

$$\boldsymbol{u}_1 - \boldsymbol{u}_0 = \boldsymbol{V}_0, \qquad \langle \boldsymbol{u}_0, \boldsymbol{e}\rangle = 0. \tag{35}$$

Since $P_0\boldsymbol{e} = P_1\boldsymbol{e} = \boldsymbol{0}$, the two equations of (34) have a solution only if

$$\langle \lambda - \mu\boldsymbol{e}, \boldsymbol{e}\rangle = 0, \qquad \langle \lambda, \boldsymbol{e}\rangle = 0, \tag{36}$$

hence $\langle \lambda, \boldsymbol{e}\rangle = 0$ and $\mu = 0$. Let P_0^+, P_1^+ as in Eq. (23), it follows from Lemma 2.2 that if Eq. (36) holds then

$$\boldsymbol{u}_0 = \sigma_0^{-1}(P_0^+)^{-1}\lambda, \qquad \boldsymbol{u}_1 = -\sigma_1^{-1}(P_1^+)^{-1}\lambda + \beta_1\boldsymbol{e}, \qquad \beta_1 \in \mathbb{R}, \tag{37}$$

are solution to (34) and $\langle \boldsymbol{u}_0, \boldsymbol{e}\rangle = 0$. The first equation of Eq. (35) yields

$$\boldsymbol{V}_0 = \boldsymbol{u}_1 - \boldsymbol{u}_0 = -(\sigma_1^{-1}(P_1^+)^{-1} + \sigma_0^{-1}(P_0^+)^{-1})\lambda + \beta_1\boldsymbol{e} = F\lambda + G\beta_1, \tag{38}$$

with matrices F, G as in Eq. (22). Together with Eq. (36) it yields system Eq. (21). Lemma 2.2 shows that $\boldsymbol{u}_0, \boldsymbol{u}_1$ are independent from α_0, α_1. From Eq. (25) follows $\langle (P_0^+)^{-1}\lambda, \boldsymbol{e}\rangle = \langle (P_1^+)^{-1}\lambda, \boldsymbol{e}\rangle = 0$ and therefore $\langle F\lambda, \boldsymbol{e}\rangle = 0$. Thus, from Eq. (38) we deduce $\langle \boldsymbol{V}_0, \boldsymbol{e}\rangle = \langle G\beta_1, \boldsymbol{e}\rangle = \beta_1\langle \boldsymbol{e}, \boldsymbol{e}\rangle$, hence also β_1 is independent from α_0, α_1. Finally, λ in independent from α_0, α_1 since $\lambda = \sigma_0 P_0\boldsymbol{u}_0$. Since $\beta_1 = \langle \boldsymbol{V}_0, \boldsymbol{e}\rangle / \langle \boldsymbol{e}, \boldsymbol{e}\rangle$ and F is negative definite (P_1^+, P_0^+ are positive definite) then λ exists and is unique, hence system Eq. (21) is well posed. □

Remark 2.3. Note that the content of this section is readily adapted to a problem Eq. (1) with unbounded domain Ω_0, hence without boundary condition (1)(h) but a vanishing condition $\|\boldsymbol{u}_0\| \to 0$ as $\|\boldsymbol{x}\| \to \infty$. In that case, P_0 is derived analogously to P_1. However, P_0 would be non-singular, hence in Theorem 2.1 we consider Eq. (23) with $\alpha_0 = 0$. Condition $\langle \lambda, \boldsymbol{e}\rangle = 0$ is still required for the existence of a solution to $\sigma_1 P_1\boldsymbol{u}_1 = -\lambda$, while $\langle \boldsymbol{u}_0, \boldsymbol{e}\rangle = 0$ is not necessary since the free constant is already fixed by the vanishing condition on $\boldsymbol{u}_0$.

3. Discretization of the full cell-by-cell model

We introduce here the general cell-by-cell model. We consider an extracellular domain $\Omega_0 \subset \mathbb{R}^d$, $d = 2$, an intracellular domain $\Omega_{\mathrm{I}} \subset \mathbb{R}^d$, and an interface domain $\Gamma_0 = \bar{\Omega}_0 \cap \bar{\Omega}_{\mathrm{I}}$. (See Fig. 2 for a graphical illustration of the model.) We suppose that Ω_{I} and Ω_0 are disjoint and we denote by Ω the whole tissue, $\Omega = \Omega_{\mathrm{I}} \cup \Omega_0 \cup \Gamma_0$. The domain Ω is always assumed connected and bounded, with $\Sigma = \partial\Omega$. For the sake of simplicity, $\partial\Omega_0 \setminus \Gamma_0 = \Sigma$ and $\partial\Omega_{\mathrm{I}} = \Gamma_0$, that is the exterior boundary of Ω

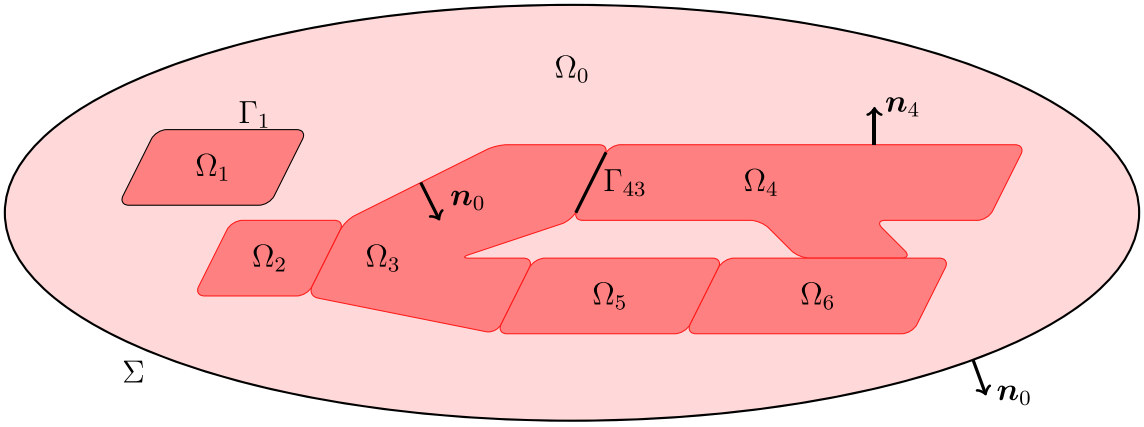

Fig. 2. Illustration of problem Eq. (39).

always corresponds to the extracellular matrix. Next, the intracellular space is described by the union of disjoint cells, denoted by Ω_i, $i = 1, \dots, N$. (Conveniently, Ω_i for $i = 0$ corresponds to the extracellular space.) Thus, $\Omega_\mathrm{I} = \bigcup_{i=1}^{N} \Omega_i$. We denote $\Gamma_i = \partial\Omega_i$, $i = 1, \dots, N$. The cell-to-cell interconnections are denoted by $\Gamma_{ij} = \Gamma_i \cap \Gamma_j$, $0 \le i, j \le N$, $i \ne j$. Note that the boundary of each cell is either in contact with another cell or with the extracellular space. The cell-by-cell model reads as follows:

$$
\begin{cases}
-\sigma_i \Delta u_i = 0, & \text{in } \Omega_i,\ i = 0, \dots, N, & \text{(a)} \\
u_i - u_0 = V_{i0}, & \text{on } \Gamma_{i0} \text{ for } 1 \le i \le N, & \text{(b)} \\
-\sigma_i \partial_{\boldsymbol{n}_i} u_i = I_\mathrm{t}(V_{i0}, z_i, t, \boldsymbol{x}), & \text{on } \Gamma_{i0} \text{ for } 1 \le i \le N, & \text{(c)} \\
-\sigma_0 \partial_{\boldsymbol{n}_0} u_0 = -I_\mathrm{t}(V_{i0}, z_i, t, \boldsymbol{x}), & \text{on } \Gamma_{i0} \text{ for } 1 \le i \le N, & \text{(d)} \\
\partial_t z_i = g(V_{i0}, z_i), & \text{on } \Gamma_{i0} \text{ for } 1 \le i \le N, & \text{(e)} \\
-\sigma_i \partial_{\boldsymbol{n}_i} u_i = \kappa(u_i - u_j), & \text{on } \Gamma_{ij} \text{ for } 1 \le i, j \le N,\ i \ne j, & \text{(f)} \\
-\sigma_0 \partial_{\boldsymbol{n}_0} u_0 = 0, & \text{on } \Sigma, & \text{(g)}
\end{cases}
\tag{39}
$$

with $I_\mathrm{t}(V_{i0}, z_i, t, \boldsymbol{x}) = C_\mathrm{m} \partial_t V_{i0} + I_\mathrm{ion}(V_{i0}, z_i) + I_\mathrm{stim}(t, \boldsymbol{x})$. The constant conductivities are $\sigma_i > 0$, $i = 0, \dots, N$. The gap junctions (intercellular connections) are represented by Γ_{ij} for $1 \le i, j \le N$, $i \ne j$, with permeability κ. The normals $\boldsymbol{n}_i$ point outwards to Ω_i. The intracellular potentials are u_i for $i = 1, \dots, N$, the extracellular potential is u_0 and V_{i0} is the transmembrane potential on Γ_{i0}. The membrane electric capacitance is C_m and I_ion represents the sum of ionic currents. The transmembrane potential V_{i0} is regulated by the ionic currents, which in turn depend on ionic concentrations and their transmembrane fluxes through ion channels, which are governed by gating variables. Ion concentrations and gating variables are represented by z_i and the pair I_ion, g describe the membrane ionic model. Several ionic models exist and they typically consist of few to hundreds of equations. We remark that there is no restriction in the system (39) for having different ionic models on each cell. In the definition of I_t, $I_\mathrm{stim}(t, \boldsymbol{x})$ is an applied stimulus on the transmembrane boundary. For the sake of simplicity and alleviate the presentation, for the time being we set $I_\mathrm{stim}(t, \boldsymbol{x}) = 0$ and drop $t, \boldsymbol{x}$ from the notation of I_t.

Model Eq. (39) is a slight simplification of a more detailed model by [4], where the dynamics at the gap junctions is time dependent and nonlinear in $u_i - u_j$. The simplification adopted here follows from linearization and an equilibrium assumption. This procedure leads to a less computationally intensive model. Solving the complete model and compare the results is subject of a future work.

In this section we adapt the techniques used in Section 2 to the full problem Eq. (39). First, in Section 3.1, we perform the spatial discretization of the cell-by-cell model, obtaining a differential–algebraic equation. Then, in Section 3.2, we reduce the problem to a system of ordinary differential equations on the transmembrane boundary.

We start rewriting Eq. (39) as follows. Let $V_{ij} = u_i - u_j$ be the difference of potential defined on the gap junctions Γ_{ij} for $1 \le j < i \le N$. Please note that we consider Γ_{ij} with $j < i$ only, this is to avoid any confusion regarding the sign of u_i and u_j in the definition of V_{ij}. Let $\Gamma_g = \cup_{1 \le j < i \le N} \Gamma_{ij}$ be the union of all gap junctions, Γ_0 is the transmembrane boundary and $\Gamma = \Gamma_0 \cup \Gamma_g$ the union of all internal boundaries. We define V on Γ by $V|_{\Gamma_{ij}} = V_{ij}$. With this definition of V, Eq. (40)(c) replaces Eq. (39)(b) and defines V on the gap junctions. Condition (39)(d) yields Eq. (40)(e), while summing Eqs. (39)(c) and (39)(d) we obtain Eq. (40)(b) for $j = 0$. Summing Eq. (39)(f) inverting the roles of i, j yields Eq. (40)(b) for $j \ge 1$, while taking the difference gives Eq. (40)(d).

$$
\begin{cases}
-\sigma_i \Delta u_i = 0, & \text{in } \Omega_i \text{ for } i = 0, \dots, N, & \text{(a)} \\
\sigma_i \partial_{\boldsymbol{n}_i} u_i + \sigma_j \partial_{\boldsymbol{n}_j} u_j = 0, & \text{on } \Gamma_{ij} \text{ for } 0 \le j < i \le N, & \text{(b)} \\
u_i - u_j = V, & \text{on } \Gamma_{ij} \text{ for } 0 \le j < i \le N, & \text{(c)} \\
\sigma_j \partial_{\boldsymbol{n}_j} u_j - \sigma_i \partial_{\boldsymbol{n}_i} u_i = 2\kappa V, & \text{on } \Gamma_{ij} \text{ for } 1 \le j < i \le N, & \text{(d)} \\
\sigma_0 \partial_{\boldsymbol{n}_0} u_0 = I_\mathrm{t}(V, z), & \text{on } \Gamma_0, & \text{(e)} \\
\partial_t z = g(V, z), & \text{on } \Gamma_0. & \text{(f)} \\
\sigma_0 \partial_{\boldsymbol{n}_0} u_0 = 0, & \text{on } \Sigma. & \text{(g)}
\end{cases}
\tag{40}
$$

Model Eq. (40) is equivalent to Eq. (39), however it is written in a more "symmetric" form.

3.1. Spatial discretization of the cell-by-cell model

We discretize all boundary segments Γ_{ij} with M_{ij} collocation points $\boldsymbol{x}_{ij}^k \in \mathring{\Gamma}_{ij}$, for $k = 1, \dots, M_{ij}$ and $0 \le j < i \le N$. Let M_i be the number of discretization points lying on boundary Γ_i, $i = 0, \dots, N$. The total number of collocation points on $\Gamma = \cup_{i=0}^{N} \Gamma_i$ is $M = \sum_{0 \le j < i \le N} M_{ij} = \frac{1}{2} \sum_{i=0}^{N} M_i$. We denote $\boldsymbol{x}^l$, $l = 1, \dots, M$, the global collocations points on Γ and by $\boldsymbol{x}_i^k$, $k = 1, \dots, M_i$, the local collocation points on Γ_i. Note that every $\boldsymbol{x}^l$ lies on some Γ_{ij}, hence there are $\boldsymbol{x}_{ij}^{k_1}$, $\boldsymbol{x}_i^{k_2}$, $\boldsymbol{x}_j^{k_3}$ satisfying $\boldsymbol{x}^l = \boldsymbol{x}_{ij}^{k_1} = \boldsymbol{x}_i^{k_2} = \boldsymbol{x}_j^{k_3}$.

Let $A_i \in \mathbb{R}^{M_i \times M}$ be the boolean connectivity matrix mapping a vector $\boldsymbol{v} \in \mathbb{R}^M$ of global nodal values on Γ to the vector $\boldsymbol{v}_i \in \mathbb{R}^{M_i}$ of local nodal values on Γ_i. Every line of A_i has exactly one non zero element: $(A_i)_{kl} = 1$ for k, l such that $\boldsymbol{x}^l = \boldsymbol{x}_i^k$. Note that $A_i^\top$ maps local to global degrees of freedom. We also define $B_i \in \mathbb{R}^{M_i \times M}$ having the same sparsity pattern as A_i. Let $(B_i)_{kl}$ be the only non zero element in the kth line, hence $\boldsymbol{x}^l = \boldsymbol{x}_i^k$. If $\boldsymbol{x}^l \in \Gamma_{ij}$ with $j < i$ then $(B_i)_{kl} = 1$, else $(B_i)_{kl} = -1$.

Let $P_i \in \mathbb{R}^{M_i \times M_i}$ be the discrete Poincaré–Steklov operator on each domain Ω_i and $\boldsymbol{u}_i \in \mathbb{R}^{M_i}$ the vector of coordinates representing $\gamma_0^\mathrm{i} u_i$. The vector of coordinates $\boldsymbol{V} \in \mathbb{R}^M$ represents V and $\boldsymbol{V}_0 = A_0 \boldsymbol{V}$ represents $V|_{\Gamma_0}$. The spatial discretization of Eqs. (40)(b) and (40)(c)

is given by

$$\sum_{i=0}^{N} \sigma_i A_i^\top P_i \boldsymbol{u}_i = \boldsymbol{0}, \qquad \sum_{i=0}^{N} B_i^\top \boldsymbol{u}_i = \boldsymbol{V}. \tag{41}$$

Recall that A_0 is the connectivity matrix mapping a global vector $\boldsymbol{v} \in \mathbb{R}^M$ to a local vector $\boldsymbol{v}_0 \in \mathbb{R}^{M_0}$ on the transmembrane boundary Γ_0. Let $M_g = M - M_0$ be the number of points on the gap junctions Γ_g and $A_g \in \mathbb{R}^{M_g \times M}$ the matrix mapping a global vector to a local vector $\boldsymbol{v}_g \in \mathbb{R}^{M_g}$ on Γ_g. The spatial discretization of Eqs. (40)(d) and (40)(e) is

$$\sigma_0 P_0 \boldsymbol{u}_0 = I_{\mathrm{t}}(A_0 \boldsymbol{V}, \boldsymbol{z}), \qquad \sum_{i=1}^{N} \sigma_i A_g B_i^\top P_i \boldsymbol{u}_i = -2\kappa A_g \boldsymbol{V}. \tag{42}$$

As in Section 2, conditions Eqs. (40)(a) and (40)(g) are automatically satisfied by the Green representation formula (3) and the definition of the Poincaré–Steklov operator P_0 on Ω_0. Finally, the spatial discretization of Eq. (40)(f) is

$$\boldsymbol{z}' = g(A_0 \boldsymbol{V}, \boldsymbol{z}). \tag{43}$$

Hence, the spatial discretization of Eq. (40) is given by Eqs. (41)–(43).

3.2. Reduction to an ordinary differential equation

In this section we transform the space discretization Eqs. (41)–(43) into an ordinary differential equation. First, similarly to Section 2.4, we search for linear maps

$$\psi_i : \mathbb{R}^M \to \mathbb{R}^{M_i}, \qquad \psi_i(\boldsymbol{V}) = \sigma_i P_i \boldsymbol{u}_i, \qquad i = 0, \dots, N, \tag{44}$$

where the $\boldsymbol{u}_i$ satisfy Eq. (41). With the help of these maps we can dispose of Eq. (41) by inserting Eq. (44) into Eq. (42) and obtain the system of equations

$$\psi_0(\boldsymbol{V}) = I_{\mathrm{t}}(A_0 \boldsymbol{V}, \boldsymbol{z}) = C_{\mathrm{m}} A_0 \boldsymbol{V}' + I_{\mathrm{ion}}(A_0 \boldsymbol{V}, \boldsymbol{z}), \qquad \sum_{i=1}^{N} A_g B_i^\top \psi_i(\boldsymbol{V}) = -2\kappa A_g \boldsymbol{V}. \tag{45}$$

However, Eq. (45) is a differential–algebraic equation (DAE), which requires more involved time marching schemes than a simple ODE. Therefore, departing from the definition of the maps ψ_i given in Theorem 3.1, in Theorem 3.2 we derive a new map which takes into account also the algebraic condition (second equality in Eq. (45)). This new map will allow us to derive an ODE instead of a DAE.

We start with the theorem below, where we compute the maps ψ_i of Eq. (44). The procedure adopted here is inspired from [31], where a domain decomposition technique for the BEM is presented.

Theorem 3.1. *The linear maps ψ_i from Eq. (44) satisfy*

$$\psi_i(\boldsymbol{V}) = -B_i \lambda, \tag{46}$$

with $\lambda \in \mathbb{R}^M$ and $\boldsymbol{\beta} \in \mathbb{R}^N$ solution to

$$\begin{pmatrix} F & G \\ G^\top & 0 \end{pmatrix} \begin{pmatrix} \lambda \\ \boldsymbol{\beta} \end{pmatrix} = \begin{pmatrix} \boldsymbol{V} \\ \boldsymbol{0} \end{pmatrix}. \tag{47}$$

The matrices $F \in \mathbb{R}^{M \times M}$, $G \in \mathbb{R}^{M \times N}$ are defined by

$$F = -\sum_{i=0}^{N} \sigma_i^{-1} B_i^\top (P_i^+)^{-1} B_i, \qquad G = (B_1^\top \boldsymbol{e}_1, \dots, B_N^\top \boldsymbol{e}_N), \tag{48}$$

$\boldsymbol{e}_i \in \mathbb{R}^{M_i}$ is the vector of ones and

$$P_i^+ = P_i + \alpha_i \boldsymbol{e}_i \boldsymbol{e}_i^\top, \tag{49}$$

with $\alpha_i > 0$, $i = 0, \dots, N$. If needed, a solution $\boldsymbol{u}_i$ for $i = 0, \dots, N$ to Eq. (41) is computed with

$$\boldsymbol{u}_i = -\sigma_i^{-1} (P_i^+)^{-1} B_i \lambda + \beta_i \boldsymbol{e}_i, \tag{50}$$

where $\boldsymbol{\beta} = (\beta_1, \dots, \beta_N)^\top$ and $\beta_0 = 0$. Furthermore, all unknowns $\lambda, \boldsymbol{\beta}, \boldsymbol{u}_i$ for $i = 0, \dots, N$ are independent from α_i, $i = 0, \dots, N$.

Proof. We consider the constrained minimization problem with Lagrangian function

$$\mathcal{L}(\boldsymbol{u}_0, \dots, \boldsymbol{u}_N, \lambda, \mu) = \sum_{i=0}^{N} \frac{\sigma_i}{2} \langle P_i \boldsymbol{u}_i, \boldsymbol{u}_i \rangle + \sum_{i=0}^{N} \langle B_i^\top \boldsymbol{u}_i, \lambda \rangle - \langle \boldsymbol{V}, \lambda \rangle + \mu \langle \boldsymbol{u}_0, \boldsymbol{e}_0 \rangle, \tag{51}$$

with $\boldsymbol{e}_0 \in \mathbb{R}^{M_0}$ a vector of ones, and show that a solution to $\nabla \mathcal{L}(\boldsymbol{u}_0, \dots, \boldsymbol{u}_N, \lambda, \mu) = \boldsymbol{0}$ solves Eq. (41) and defines ψ_i. Hence, we impose

$$\nabla_{\boldsymbol{u}_0} \mathcal{L}(\boldsymbol{u}_0, \dots, \boldsymbol{u}_N, \lambda, \mu) = \sigma_0 P_0 \boldsymbol{u}_0 + B_0 \lambda + \mu \boldsymbol{e}_0 = \boldsymbol{0}, \tag{52a}$$

$$\nabla_{\boldsymbol{u}_i} \mathcal{L}(\boldsymbol{u}_0, \dots, \boldsymbol{u}_N, \lambda, \mu) = \sigma_i P_i \boldsymbol{u}_i + B_i \lambda = \boldsymbol{0}, \quad i = 1, \dots, N, \tag{52b}$$

$$\nabla_{\lambda} \mathcal{L}(\boldsymbol{u}_0, \dots, \boldsymbol{u}_N, \lambda) = \sum_{i=0}^{N} B_i^\top \boldsymbol{u}_i - \boldsymbol{V} = \boldsymbol{0}, \tag{52c}$$

$$\nabla_{\mu} \mathcal{L}(\boldsymbol{u}_0, \dots, \boldsymbol{u}_N, \lambda, \mu) = \langle \boldsymbol{u}_0, \boldsymbol{e}_0 \rangle = 0. \tag{52d}$$

First, we notice that a solution to Eqs. (52a) and (52b) exists if and only if

$$\langle B_0 \lambda + \mu \boldsymbol{e}_0, \boldsymbol{e}_0 \rangle = 0, \qquad \langle B_i \lambda, \boldsymbol{e}_i \rangle = 0, \quad i = 1, \dots, N. \tag{53}$$

Since $\sum_{i=0}^{N} B_i^\top \boldsymbol{e}_i = \boldsymbol{0}$ (for every $+1$ there is a -1), then $\langle B_0 \lambda, \boldsymbol{e}_0 \rangle = -\sum_{i=1}^{N} \langle B_i \lambda, \boldsymbol{e}_i \rangle$. Hence, Eq. (53) is replaced with

$$\mu = 0, \qquad \langle B_i \lambda, \boldsymbol{e}_i \rangle = 0, \quad i = 1, \dots, N. \tag{54}$$

Notice that Eqs. (52a) and (52b) define $\psi_i(\boldsymbol{V}) = -B_i \lambda$. Also, imposing $\nabla \mathcal{L}(\boldsymbol{u}_0, \dots, \boldsymbol{u}_N, \lambda, \mu) = \boldsymbol{0}$ we obtain a solution to Eq. (41). Indeed, Eq. (52c) is equivalent to the second equality in Eq. (41). The first equality of Eq. (41) follows from Eqs. (52a) and (52b), indeed

$$\boldsymbol{0} = \sum_{i=0}^{N} A_i^\top \nabla_{\boldsymbol{u}_i} \mathcal{L}(\boldsymbol{u}_0, \dots, \boldsymbol{u}_N, \lambda, \mu) = \sum_{i=0}^{N} \sigma_i A_i^\top P_i \boldsymbol{u}_i + A_i^\top B_i \lambda = \sum_{i=0}^{N} \sigma_i A_i^\top P_i \boldsymbol{u}_i, \tag{55}$$

where we used $\sum_{i=0}^{N} A_i^\top B_i = 0$ (for every 1 there is a -1) and $\mu = 0$.

It remains to find a solution to Eq. (52). If Eq. (54) is satisfied, a solution $\boldsymbol{u}_i$ to Eqs. (52a), (52b) and (52d) exists and is given by

$$\boldsymbol{u}_0 = -\sigma_0^{-1} (P_0^+)^{-1} B_0 \lambda, \qquad \boldsymbol{u}_i = -\sigma_i^{-1} (P_i^+)^{-1} B_i \lambda + \beta_i \boldsymbol{e}_i, \tag{56}$$

with $P_i^+ = P_i + \alpha_i \boldsymbol{e}_i \boldsymbol{e}_i^\top$, $\alpha_i > 0$ and $\beta_i \in \mathbb{R}$, $i = 1, \dots, N$. To compute λ and $\boldsymbol{\beta} = (\beta_1, \dots, \beta_N)$, we insert Eq. (56) into Eq. (52c), yielding

$$\boldsymbol{V} = \sum_{i=0}^{N} B_i^\top (-\sigma_i^{-1} (P_i^+)^{-1} B_i \lambda + \beta_i \boldsymbol{e}_i) = -\sum_{i=0}^{N} \sigma_i^{-1} B_i^\top (P_i^+)^{-1} B_i \lambda + \sum_{i=1}^{N} \beta_i B_i^\top \boldsymbol{e}_i, \tag{57}$$

with $\beta_0 = 0$. From Eqs. (54) and (57) follows Eq. (47). Since all $\boldsymbol{u}_i$ are independent from the α_i, then also λ (cf. Eqs. (52a) and (52b)) and $\boldsymbol{\beta}$ ($\beta_i M_i = \langle \boldsymbol{u}_i, \boldsymbol{e}_i \rangle$).

To show the invertibility of Eq. (47) it is sufficient to prove that F is negative definite and that G has full column rank [32, Section 3.2].

Since P_i^+ are positive definite, then

$$\begin{aligned} -\lambda^\top F \lambda &= \sum_{i=0}^{N} \sigma_i^{-1} (B_i \lambda)^\top (P_i^+)^{-1} B_i \lambda \geq C \min_{i=0,\dots,N} \sigma_i^{-1} \sum_{i=0}^{N} \|B_i \lambda\|^2 \\ &= 2C \min_{i=0,\dots,N} \sigma_i^{-1} \|\lambda\|^2, \end{aligned} \tag{58}$$

since $\sum_{i=0}^{N} \|B_i \lambda\|^2 = 2\|\lambda\|^2$. Hence, F is negative definite. Furthermore,

$$\begin{aligned} \|G\boldsymbol{\beta}\|^2 &= \sum_{i,j=1}^{N} \beta_i \beta_j \langle B_i^\top \boldsymbol{e}_i, B_j^\top \boldsymbol{e}_j \rangle = \sum_{i=1}^{N} \beta_i^2 M_i - \sum_{i,j=1, i \neq j}^{N} \beta_i \beta_j M_{ij} \\ &= \sum_{i=1}^{N} \beta_i^2 \left(M_{0i} + \sum_{j=1, j \neq i}^{N} M_{ij} \right) - \sum_{i,j=1, i \neq j}^{N} \beta_i \beta_j M_{ij} \end{aligned} \tag{59}$$

$$= \sum_{i=1}^{N} \beta_i^2 M_{0i} + \sum_{i,j=1, i\neq j}^{N} (\beta_i^2 - \beta_i\beta_j) M_{ij} \tag{60}$$

$$= \sum_{i=1}^{N} \beta_i^2 M_{0i} + \frac{1}{2} \sum_{i,j=1, i\neq j}^{N} (\beta_i^2 + \beta_j^2 - 2\beta_i\beta_j) M_{ij}$$

$$= \sum_{i=1}^{N} \beta_i^2 M_{0i} + \frac{1}{2} \sum_{i,j=1, i\neq j}^{N} (\beta_i - \beta_j)^2 M_{ij} \tag{61}$$

$$\geq \min_{i=1,\dots,N} M_{0i} \|\boldsymbol{\beta}\|^2. \tag{62}$$

and thus G has full column rank. □

Now we use the result of Theorem 3.1 and the second equality of Eq. (45) in order to derive a standard ODE problem. We recall that $\boldsymbol{V}_0 = A_0 \boldsymbol{V}$.

Theorem 3.2. *The space discretization Eqs. (41)–(43) of Eq. (39) is equivalent to the ordinary differential equations system*

$$\begin{cases} C_m \boldsymbol{V}_0' + I_{ion}(\boldsymbol{V}_0, \boldsymbol{z}) = \psi(\boldsymbol{V}_0), & (a) \\ \boldsymbol{z}' = g(\boldsymbol{V}_0, \boldsymbol{z}), & (b) \end{cases} \tag{63}$$

where $\psi(\boldsymbol{V}_0) = \lambda_0$ *and* $\lambda_0 \in \mathbb{R}^{M_0}$, $\lambda_g \in \mathbb{R}^{M_g}$, $\boldsymbol{\beta} \in \mathbb{R}^N$ *are solutions to*

$$\begin{pmatrix} F_{00} & F_{0g} & A_0 G \\ F_{g0} & F_{gg} - \kappa^{-1} I & A_g G \\ G^\top A_0^\top & G^\top A_g^\top & 0 \end{pmatrix} \begin{pmatrix} \lambda_0 \\ \lambda_g \\ \boldsymbol{\beta} \end{pmatrix} = \begin{pmatrix} \boldsymbol{V}_0 \\ \boldsymbol{0} \\ \boldsymbol{0} \end{pmatrix}, \tag{64}$$

with

$$F_{00} = A_0 F A_0^\top, \quad F_{0g} = A_0 F A_g^\top, \quad F_{g0} = A_g F A_0^\top, \quad F_{gg} = A_g F A_g^\top, \tag{65}$$

and matrices F, G *defined in Eq. (48).*

Proof. We denote $\boldsymbol{V}_g = A_g \boldsymbol{V}$, $\boldsymbol{V}_0 = A_0 \boldsymbol{V}$, $\lambda_g = A_g \lambda$ and $\lambda_0 = A_0 \lambda$. Also, note that $B_i^\top B_i = A_i^\top A_i$ since $B_i^\top B_i$ projects a global vector forth and back from Γ_i and if a sign change happens it occurs twice. Therefore

$$\left(\sum_{i=0}^{N} B_i^\top B_i \right) \boldsymbol{v} = \left(\sum_{i=0}^{N} A_i^\top A_i \right) \boldsymbol{v} = 2\boldsymbol{v} \qquad \forall\, \boldsymbol{v} \in \mathbb{R}^M, \tag{66}$$

indeed every segment Γ_{ij} will receive the contribution from exactly two neighboring domains. From Theorem 3.1 we have that $\psi_i(\boldsymbol{V}) = -B_i \lambda$, which inserted into the second equality of Eq. (45) yields

$$\kappa \boldsymbol{V}_g = \kappa A_g \boldsymbol{V} = -\frac{1}{2} \sum_{i=1}^{N} A_g B_i^\top \psi_i(\boldsymbol{V}) = \frac{1}{2} A_g \left(\sum_{i=0}^{N} B_i^\top B_i \right) \lambda = A_g \lambda = \lambda_g. \tag{67}$$

Note as well that $A_0^\top A_0 + A_g^\top A_g$ is the identity matrix in $\mathbb{R}^M$, hence multiplying the first line $F\lambda + G\boldsymbol{\beta} = \boldsymbol{V}$ of Eq. (47) with A_0 yields

$$\boldsymbol{V}_0 = A_0 \boldsymbol{V} = A_0 F (A_0^\top A_0 \lambda + A_g^\top A_g \lambda) + A_0 G \boldsymbol{\beta} = F_{00} \lambda_0 + F_{0g} \lambda_g + A_0 G \boldsymbol{\beta}. \tag{68}$$

Similarly, multiplication by A_g yields $\boldsymbol{V}_g = F_{g0} \lambda_0 + F_{gg} \lambda_g + A_g G \boldsymbol{\beta}$ and thus

$$\boldsymbol{0} = F_{g0} \lambda_0 + (F_{gg} - \kappa^{-1} I) \lambda_g + A_g G \boldsymbol{\beta}. \tag{69}$$

For the second line of Eq. (47) we have

$$\boldsymbol{0} = G^\top \lambda = G^\top A_0^\top \lambda_0 + G^\top A_g^\top \lambda_g. \tag{70}$$

Relations Eqs. (68) to (70) yield Eq. (64). The identity $-B_0 = A_0$ and $\psi_0(\boldsymbol{V}) = -B_0 \lambda = A_0 \lambda = \lambda_0$ implies $\psi_0(\boldsymbol{V}) = \psi(\boldsymbol{V}_0)$ and hence Eq. (63).

Invertibility of Eq. (64) follows from the same reasoning as in Theorem 3.1 for Eq. (47). Indeed, the upper-left 2×2 block is a simple row-column permutation of F plus $-\kappa^{-1}$ on some diagonal terms. Hence, the upper-left 2×2 block remains negative definite, whereas G is replaced by a row permutation of itself and therefore remains full column rank. □

From the proof of Theorem 3.2 we see that $\boldsymbol{V}$, λ of Theorem 3.1 are given by $\boldsymbol{V} = A_0^\top \boldsymbol{V}_0 + A_g^\top \boldsymbol{V}_g$, $\lambda = A_0^\top \lambda_0 + A_g^\top \lambda_g$, $\kappa \boldsymbol{V}_g = \lambda_g$ and moreover $\boldsymbol{\beta}$ is the same as in Theorem 3.1; hence, if needed, $\boldsymbol{u}_i$ for $i = 0, \dots, N$ can be computed as in Theorem 3.1. Note as well that in Eq. (64) we have chosen to use λ_g as unknown, instead of the alternative $\boldsymbol{V}_g$. If we used $\boldsymbol{V}_g$ we would obtain the same matrix as in Eq. (64) but with the second column multiplied by κ and therefore break the symmetry.

We remark that the operator ψ can be represented by a dense matrix, just by inverting Eq. (64). This is numerically convenient only for relatively small problems, as those presented below. A more efficient strategy would be to approximate the action of ψ by some preconditioned iterative scheme. Interestingly, block preconditioners could be related to operator splitting, which is an efficient way to solve the EMI model with the Finite Element Method [33].

3.3. Time integration

For the time integration of Eq. (63), we use the multirate explicit stabilized method mRKC [34,35] for problems

$$\boldsymbol{y}' = f_F(t, \boldsymbol{y}) + f_S(t, \boldsymbol{y}), \qquad \boldsymbol{y}(0) = \boldsymbol{y}_0, \tag{71}$$

where f_F is a stiff term and f_S is a mildly stiff but more expensive term. Instead of Eq. (71), the method solves a modified problem

$$\boldsymbol{y}_\eta' = f_\eta(\boldsymbol{y}_\eta), \tag{72}$$

where f_η is an averaged right-hand side. Evaluation of $f_\eta(\boldsymbol{y}_\eta)$ requires the solution to an auxiliary problem

$$\boldsymbol{u}' = f_F(\boldsymbol{u}) + f_S(\boldsymbol{y}_\eta), \quad t \in (0, \eta), \qquad \boldsymbol{u}(0) = \boldsymbol{y}_\eta, \qquad f_\eta(\boldsymbol{y}_\eta) = \frac{1}{\eta}(\boldsymbol{u}(\eta) - \boldsymbol{y}_\eta), \tag{73}$$

where $\eta > 0$ depends on the step size Δt and the stiffness of f_F, f_S; in general, η is significantly smaller than Δt [34]. Both Eqs. (72) and (73) are solved with Runge–Kutta–Chebyshev (RKC) methods.

The mRKC scheme is first-order accurate, fully explicit and does not have any step size restriction. Its stability properties are inherited from the RKC methods [36], which use an increased number of stages, with respect to classical methods, to increase stability (instead of accuracy). Since the stability domain's size grows quadratically with the number of function evaluations, the methods are particularly efficient. The advantage of mRKC with respect to a standard RKC scheme is that the stiffness of f_η is comparable to the one of the slow term f_S; hence, Eq. (72) is cheaper to solve than Eq. (71). Moreover, the evaluations of f_η or $f_F + f_S$ have similar costs, since in Eq. (73) the expensive term f_S is frozen and η is in general small. Due to the auxiliary problem, the number of function evaluations of f_F, f_S needed for stability is decoupled and depends only on their own stiffness. In contrast, the RKC method evaluates f_F, f_S concurrently, hence the evaluations of the expensive term f_S depend on the stiffness of f_F.

For the integration of Eq. (63) with mRKC, we rewrite Eq. (63) as Eq. (71), with

$$\boldsymbol{y} = \begin{pmatrix} \boldsymbol{V}_0 \\ \boldsymbol{z} \end{pmatrix}, \qquad f_F(t, \boldsymbol{y}) = \begin{pmatrix} \psi(\boldsymbol{V}_0)/C_m \\ \boldsymbol{0} \end{pmatrix},$$
$$f_S(t, \boldsymbol{y}) = \begin{pmatrix} -(I_{ion}(\boldsymbol{V}_0, \boldsymbol{z}) + I_{stim}(t))/C_m \\ g(\boldsymbol{V}_0, \boldsymbol{z}) \end{pmatrix}, \tag{74}$$

where $I_{stim}(t)$ is a vector used to apply a stimulus locally and initiate an action potential propagation. In our simulations Eq. (64) is factorized once, hence evaluation of f_F reduces to a matrix vector multiplication and is very cheap. In contrast, f_S contains evaluation of the ionic model, which is expensive due to the increased number of variables and nonlinearities.

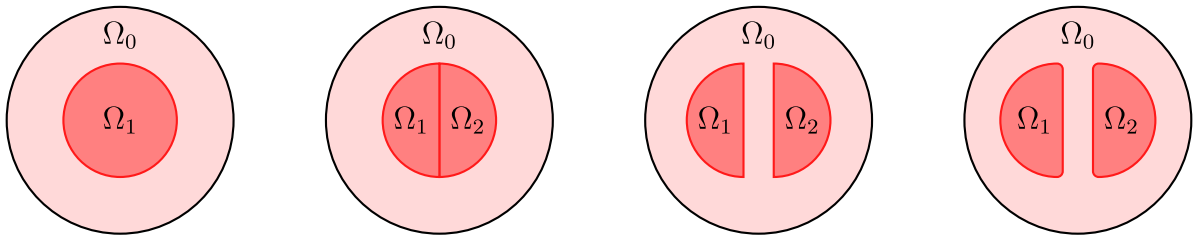

(a) Single cell (b) Two cells (c) Isolated, non-smooth cells (d) Isolated, smooth cells

Fig. 3. Illustration of the geometrical settings employed in Section 4.1.

Table 1
Model's coefficients employed in numerical experiments.

C_m	σ_0	$\sigma_1, \dots, \sigma_N$	κ
$1\,\mu\text{F}\,\text{cm}^{-2}$	$20\,\text{mS}\,\text{cm}^{-1}$	$3\,\text{mS}\,\text{cm}^{-1}$	$690\,\text{mS}\,\text{cm}^{-2}$

4. Numerical experiments

In this section we perform some numerical experiments in order to asses the accuracy of the space–time discretization of the cell-by-cell model (39) but also investigate the regularity properties of the model itself.

We start with two experiments, in Sections 4.1 and 4.2, where we investigate the convergence rates of the maps ψ_i from Theorem 3.1 and then the impact of the mesh and step size on the accuracy of the conduction velocity (CV). These experiments are crucial to understand which discretization parameters yield solutions within a certain error tolerance.

In the subsequent experiments the goal is to study the model itself. For instance, in Section 4.3 we investigate the effect of the gap junction's permeability κ on the CV and in Section 4.4 we study how the contact area between cells affects CV. Before presenting the results, we resume here below our computational setting.

Computational setup. The following numerical experiments have been performed with our C++ code [37], where for the dense linear algebra routines we employ the `Eigen` library [38]. The ionic model, is taken from `CellML` [39] and the relative C code is produced with the `Myokit` library [40]. Concerning the model Eq. (39), the number of cells N and the domains Ω_i vary from one experiment to another and are specified later. If not stated otherwise, in the next experiments we use the coefficients C_m, σ_i, κ, given in Table 1. The values for C_m, σ_i, κ are taken from [9], where for κ we consider $\kappa = 1/R_m$ with $R_m = 0.00145\ \text{k}\Omega\,\text{cm}^2$. If not specified, we consider the ionic model from Courtemanche et al. [41]. The initial values for V for and the ionic model's state variables are uniform on the transmembrane boundary and are taken from the `Myokit`'s code. For instance, for the Courtemanche-Nattel-Ramiréz model the initial value for V is $V_0 = -81.18$ mV.

4.1. Approximation properties of the ψ operators

In this experiment we investigate the convergence rate of the ψ_i operators defined in Theorem 3.1, hence only Eq. (41) plays a role, but not Eqs. (42) and (43). For this purpose, we conduct four convergence experiments, one for every geometry displayed in Fig. 3, and we display the errors on the trace and normal derivative against the number of degrees of freedom M in Fig. 4.

Let us describe the geometries of Fig. 3. In Fig. 3(a) we have a model composed of one cell ($N = 1$), defined by $\Omega_0 = \{\boldsymbol{x} \in \mathbb{R}^2 : 2 < \|\boldsymbol{x}\| < 4\}$ and $\Omega_1 = \{\boldsymbol{x} \in \mathbb{R}^2 : \|\boldsymbol{x}\| < 2\}$. In Fig. 3(b) we split the cell by introducing a vertical gap junction, hence we have the same Ω_0 but $\Omega_1 = \{\boldsymbol{x} \in \mathbb{R}^2 : \|\boldsymbol{x}\| < 2, x_1 < 0\}$ and $\Omega_2 = \{\boldsymbol{x} \in \mathbb{R}^2 : \|\boldsymbol{x}\| < 2, x_1 > 0\}$. In Fig. 3(c) we keep the same cells but remove the gap junction by introducing a horizontal gap of size 0.4 between Ω_1 and Ω_2. Finally, in Fig. 3(d) we keep the separation of Ω_1, Ω_2 but smooth out the corners by introducing quarter of circles of radius 0.2.

For the setting of Figs. 3(a) and 3(b) an exact solution to Eqs. (40)(a) to (40)(d), with V defined by Eq. (40)(c), is given by

$$u_0(\boldsymbol{x}) = \frac{\sigma_1}{\sigma_0}\frac{16 + \|\boldsymbol{x}\|^2}{6\|\boldsymbol{x}\|^2}x_2, \qquad u_1(\boldsymbol{x}) = u_2(\boldsymbol{x}) = -\frac{1}{2}x_2. \tag{75}$$

Therefore, for different values of M (i.e. number of collocation points), we can compute the vector of coefficients $\boldsymbol{u}_i$, define $\boldsymbol{V}$ as in Eq. (41), solve Eq. (47) and compute the errors

$$e_1 = \max_{i=0,\dots,N} \|\psi_i(\boldsymbol{V}) - \sigma_i \partial_{\boldsymbol{n}_i} u_i\|_{L^2(\Gamma_i)}, \qquad e_0 = \max_{i=0,\dots,N} \|\widetilde{\psi}_i(\boldsymbol{V}) - u_i\|_{L^2(\Gamma_i)/\mathbb{R}}, \tag{76}$$

where $\widetilde{\psi}_i(\boldsymbol{V}) = -\sigma_i^{-1}(P_i^+)^{-1}B_i\lambda + \beta_i e_i$ approximates u_i (cf. Eq. (50)), up to a constant.

For the geometries of Figs. 3(c) and 3(d) we do not possess an exact solution. Hence, we set $V(\boldsymbol{x}) = \cos(\pi x_1)\sin(\pi x_2)$ and errors e_1, e_0 are now computed as

$$e_1 = \max_{i=0,\dots,N} \|\psi_i(\boldsymbol{V}) - \psi_i(\boldsymbol{V}^*)\|_{L^2(\Gamma_i)}, \qquad e_0 = \max_{i=0,\dots,N} \|\widetilde{\psi}_i(\boldsymbol{V}) - \widetilde{\psi}_i(\boldsymbol{V}^*)\|_{L^2(\Gamma_i)/\mathbb{R}}, \tag{77}$$

where $\psi_i(\boldsymbol{V}^*)$, $\widetilde{\psi}_i(\boldsymbol{V}^*)$ are reference solutions calculated on a finer mesh.

We display the errors e_0, e_1 with respect to M, for the geometries of Fig. 3, in Fig. 4. Due to the smoothness of the solutions and the boundaries, we remark in Fig. 4a that for the first problem we obtain exponential convergence thanks to the trigonometric Lagrange basis functions; with very few degrees of freedom machine precision is achieved. This result is in line with the theory and experiments performed in [22]. In the second problem, the boundary is Lipschitz continuous only, which prevents exponential convergence. Indeed, in Fig. 4b the convergence rates for the trace and normal derivative are 1.5 and 0.5, respectively.

In Fig. 4a,b we see how the convergence rates decrease dramatically when the circle is divided into two half-circles. The purpose of two last experiments is to demonstrate numerically that this phenomenon is due to the non smooth boundaries, rather than the introduction of a gap junction. Indeed, in Fig. 4c we observe the same convergence rates as in Fig. 4b, while in Fig. 4d we obtain higher convergence rates.

4.2. Impact of discretization parameters on conduction velocity

It is already known that discretization methods, mesh size and step size affect conduction velocity (CV) in the monodomain and bidomain models for cardiac electrophysiology [42–44]. In this experiment we investigate how mesh and step size affect the CV for the cell-by-cell model discretized with the BEM in space and the mRKC method [34] in time. In order to be able to employ relatively uniform mesh sizes in this experiment we consider rectangular cells.

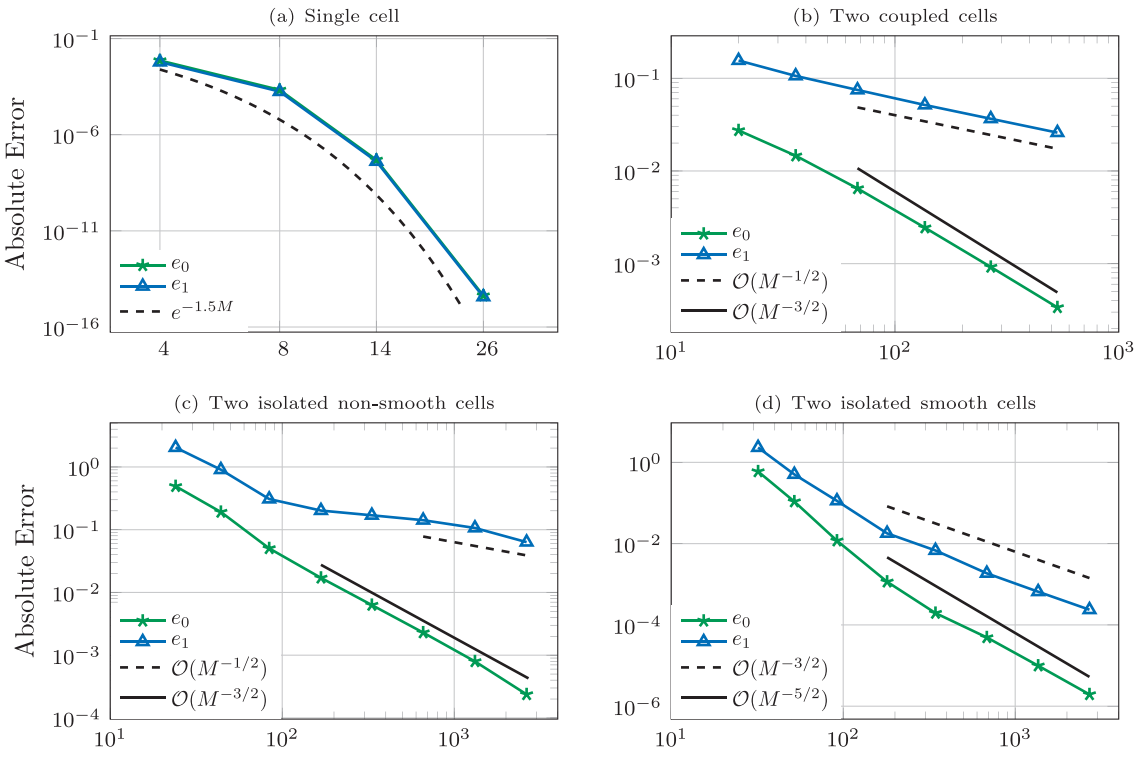

Fig. 4. Convergence rates of the ψ operator defined in Theorem 3.1 for the problems depicted in Fig. 3.

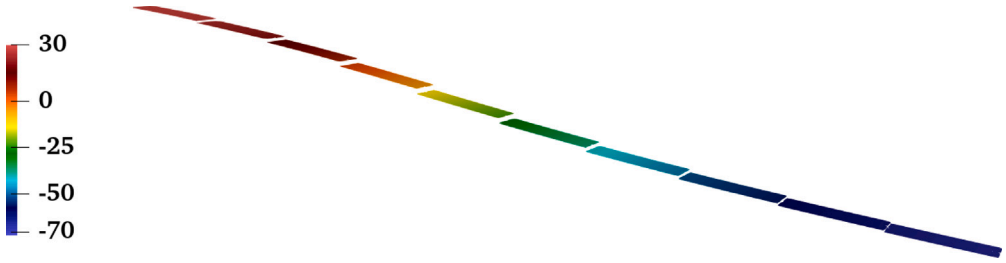

Fig. 5. Simulation of an array of 2×10 cells stimulated on the two leftmost cells. We show the inner potentials u_i, $i = 1, \dots, 20$ at $t = 1$ ms. To increase the gap between cells, and only for visualization purposes, we set $\kappa = 0.1\,\mathrm{mS\,cm^{-2}}$.

To measure the CV we design the following experiment. We consider an array of 2×30 connected rectangular cells of width $c_w = 20\,\mu\mathrm{m}$ and length $c_l = 100\,\mu\mathrm{m}$, cells are positioned so that their bottom left vertex has coordinates $(i \cdot c_l, j \cdot c_w)$ for $i = 0, \dots, 29$, $j = 0, 1$; yielding a block of cells of width $2 \cdot c_w = 40\,\mu\mathrm{m}$ and length $30 \cdot c_l = 3000\,\mu\mathrm{m}$. The outer domain is a rectangle of size $440\,\mu\mathrm{m} \times 5000\,\mu\mathrm{m}$ centered on the array of cells. To initiate an action potential traversing the cell's array a stimulus of $300\,\mu\mathrm{A\,cm^{-2}}$ is applied for a duration of 1 ms at the transmembrane boundary of the two leftmost cells. To do so, in this part of the domain and during the first 1 ms of simulation, $I_{\mathrm{ion}}(\boldsymbol{V}_0, \boldsymbol{z})$ is replaced with $I_{\mathrm{ion}}(\boldsymbol{V}_0, \boldsymbol{z}) + 300$. CV is computed as the average over $CV_k = \|\boldsymbol{p}_k - \boldsymbol{q}_k\| / (t_{p_k} - t_{q_k})$ for $k = 1, \dots, 5$, where: $\boldsymbol{p}_k = ((7.5 + k) \cdot c_l)\,\mu\mathrm{m}$, $\boldsymbol{q}_k = ((17.5 + k) \cdot c_l, 0)\,\mu\mathrm{m}$ and t_{p_k}, t_{q_k} are the time instants in which V exceeds the threshold of $V_{\mathrm{th}} = -20\,\mathrm{mV}$ in $\boldsymbol{p}_k$, $\boldsymbol{q}_k$, respectively. The choice of $\boldsymbol{p}_k$, $\boldsymbol{q}_k$ is such that measures are taken sufficiently far from the stimulated point and to avoid boundary effects as well. See Fig. 5 for an illustration of a typical solution of the cell-by-cell model. There, we simulate a shorter array of 2×10 cells, stimulated on the left as described above, and with decreased permeability $\kappa = 0.1\,\mathrm{mS\,cm^{-2}}$. We decreased the number of cells and κ only for visualization purposes: number of cells to fit the page and κ to increase the gap between cells.

We solve Eq. (63) with different step sizes $\Delta t \leq 100$ μs and mesh size $\Delta x \leq 20$ μm. However, even for large Δx we place at least two collocation points inside each segment. Hence, on the short side of the cell the local mesh size satisfies $\Delta x \leq c_w/3 \approx 6.6$ μm. For every choice of $\Delta t, \Delta x$, we compute the signed relative error on CV: $E_{\mathrm{CV}} = (\mathrm{CV} - \mathrm{CV}^*)/\mathrm{CV}^*$, with CV^* a reference solution. We display E_{CV} as function of Δt, Δx in Fig. 6. The reference value of CV is $\mathrm{CV}^* \approx 1.27153$.

First, we notice that for coarse space grids the true CV^* tends to be overestimated, whereas for large time steps it is underestimated. Then, we remark that even with relatively large mesh sizes $\Delta x = 20\,\mu\mathrm{m}$ the estimated CV remains within a 2% error. Fig. 6 (middle and right panels) also shows the same results, but for the unsigned relative error $|E_{\mathrm{CV}}|$ and fixing either Δx or Δt. We observe that the local minimal appearing in the curves is due to the cancellation of the positive spatial discretization error with the negative time discretization error.

Based on the results of this section, in the forthcoming experiments we consider $\Delta t \leq 0.02$ ms and $\Delta x \leq 10\,\mu\mathrm{m}$, which, for this experiment, yield a relative error of less than 5%.

4.3. Dependence of conduction velocity on gap junctions' permeability and cells inner conductivity

In this experiment we study how CV depends on the gap junctions' permeability κ and the inner conductivity σ_i, $i = 1, \dots, N$. For that purpose, we consider again an array of 2×30 cells and cells of size

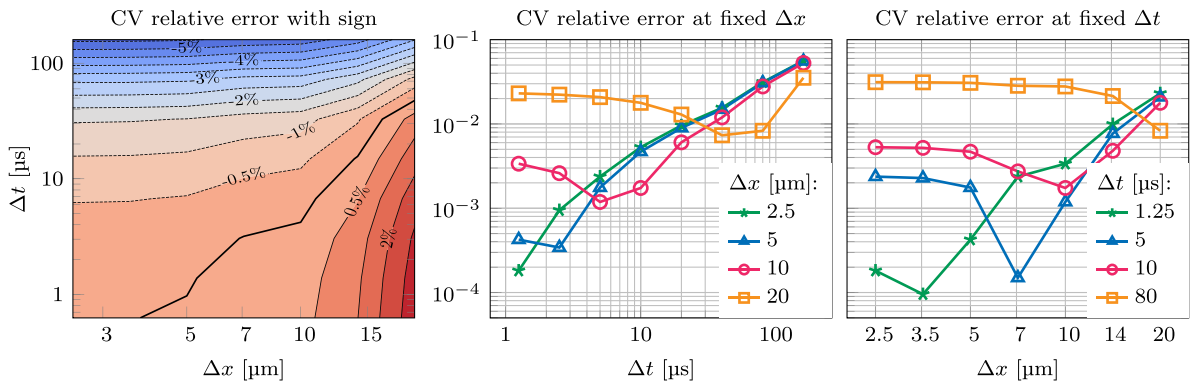

Fig. 6. Conduction velocity accuracy with respect to timestep Δt and mesh size Δx.

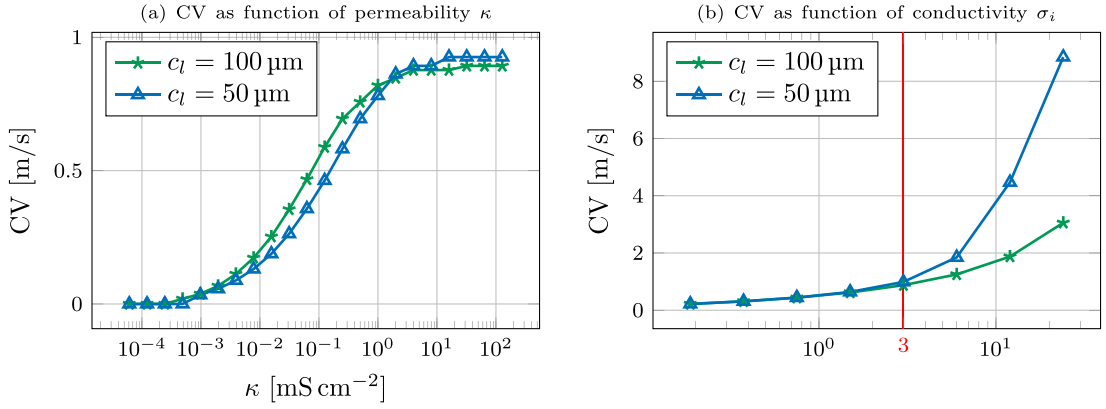

Fig. 7. Dependence of CV (in m/s) on permeability κ and intracellular conductivity σ_i (red: reference value).

$c_w \times c_l$, with fixed $c_w = 10\,\mu m$ and either $c_l = 100\,\mu m$ or $c_l = 50\,\mu m$. First, we measure CV for varying κ but keeping the other coefficients fixed. We initiate action potential propagation applying a stimulus of $200\,\mu A\,cm^{-2}$ to the transmembrane boundary of the two leftmost cells for the duration of 1 ms, similarly to Section 4.2. Results for $c_l = 100\,\mu m$ and $c_l = 50\,\mu m$ are displayed in Fig. 7a. We observe as CV decreases with κ and also that the physiological value $\kappa = 690$ is in the range where CV is maximal. We note that for values of $\kappa \leq 2 \cdot 10^{-4}$ the action potential does not propagate. Then, we measure CV for varying σ_i, $i = 1, \dots, N$, and fixed κ, results are displayed in Fig. 7b for $c_l = 100\,\mu m$ and $c_l = 50\,\mu m$. Conduction velocity increases with σ_i, specially for the shorter cells.

4.4. Dependence of conduction velocity on gap junctions' surface area

In general, gap junctions perpendicular to the fiber direction are not flat surfaces and are better modeled by intercalated discs [19]. Modeling gap junctions is not trivial, and many factor can affect the CV [45,46]. Here, we model these gap junctions with a sinus wave (see Fig. 8(a) for an illustration) of amplitude a and frequency k. For this experiment we use a mesh size of $\Delta x = 1.5$ µm on the long side of the cells, while on the sinusoidal wave we employ a local mesh size $\Delta x = \min(1.5, \ell/32/k)$ µm, where ℓ is the length of the sinusoidal wave.

In this experiment we consider and array of 2×30 cells of size $10\,\mu m \times 100\,\mu m$ and measure CV as in Section 4.2. In Fig. 8(b) we show the conductive velocity as a function of the frequency k for a fixed amplitude of $a = 0.5\,\mu m$. We note that for moderate frequency k the CV increases due to an increase of contact surface area. However, for larger frequencies CV decreases, probably because of a flux saturation at the narrower junctions. In Fig. 8(c) we show the conductive velocity as a function of the amplitude a for a fixed frequency of $k = 3$. Again, for larger amplitude a the conduction velocity decreases.

4.5. Dependence of conduction velocity on cells size and aspect ratio

Finally, we investigate how the cell's size and aspect ratio impact the conduction velocity. We consider an array of 2×30 cells of size $c_w \times c_l$. First, we fix $c_w = 10\,\mu m$ and vary c_l, results are reported in Fig. 9b. We observe as CV decreases as c_l increases. In Fig. 9a we display the results for fixed $c_l = 100\,\mu m$ and varying c_w, here CV increases with c_w. In the last figure Fig. 9c we vary both c_l and c_w while keeping a constant aspect ratio $c_l = 10 \cdot c_w$, more precisely they vary from $(c_w, c_l) = (2.5\,\mu m, 25\,\mu m)$ to $(c_w, c_l) = (14\,\mu m, 140\,\mu m)$. We see as CV increases with the cells area $A = c_l \cdot c_w$. A more in-depth study on the effect of cell size and geometry has been presented by Jæger et al. [47], where also an inhomogeneous membrane distribution of sodium channels is considered [48].

5. Conclusion

In this paper we solve the cell-by-cell or EMI model for cardiac electrophysiology via the boundary element method, with no geometrical restrictions. The cell-by-cell model consists in Laplace equations inside and outside the cellular domains coupled with an ordinary differential equation on the transmembrane boundary and an algebraic condition on the gap junctions. Due to the boundary integral formulation, Laplace equations are cleared away, yielding a differential–algebraic equation living on the cell's boundaries only. Since it is not necessary to have degrees of freedom inside each domain, our method has a lower memory footprint for storing the solution. This can be advantageous for problems where the extracellular space is large or even unbounded. In a subsequent step, the differential–algebraic equation is reduced to an ordinary differential equation lying on the transmembrane boundary only. Finally, we provide numerical results where: first, we study the

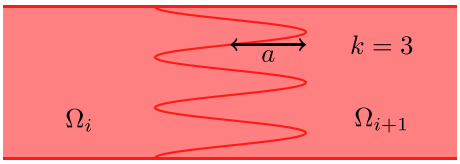

(a) Two cells with an intercalated discs at gap junctions.

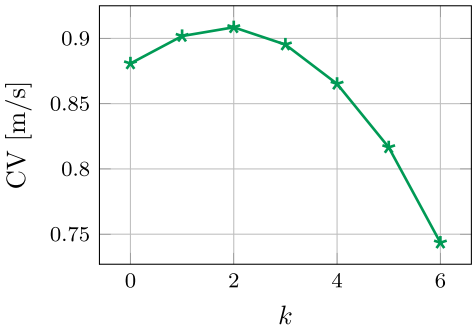

(b) Impact of intercalated discs frequency on CV for $a = 0.5\,\mu m$.

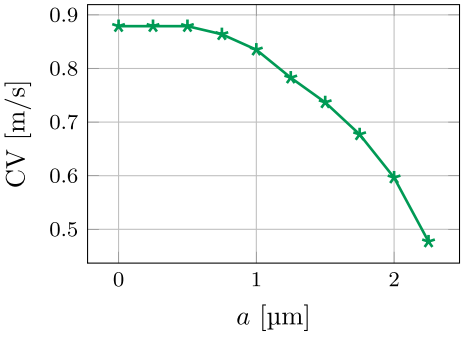

(c) Impact of intercalated discs amplitude on CV for $k = 3$.

Fig. 8. Effect of gap junctions surface area on CV (in m/s).

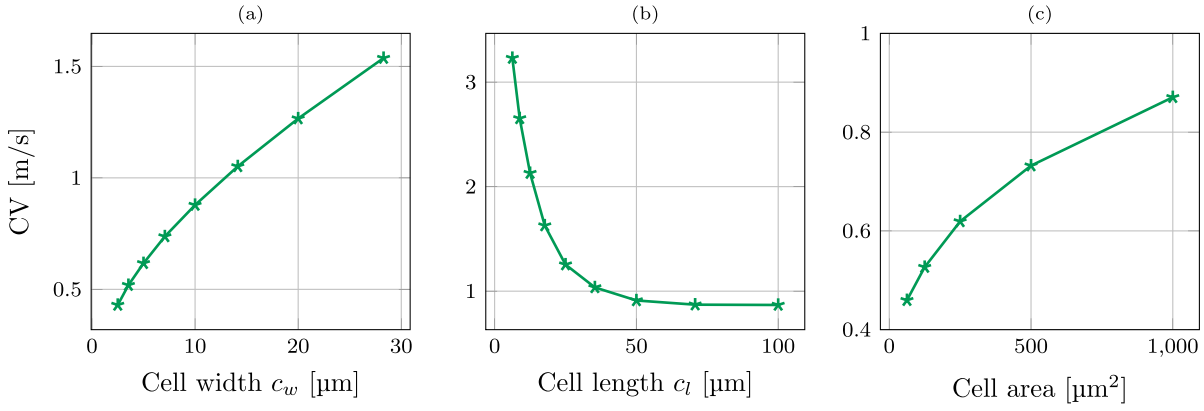

Fig. 9. Impact of cell length c_l, cell width c_w, and cell area with fixed aspect ratio on the CV (in m/s).

accuracy of the numerical method and then we investigate the model properties and sensibility with respect to its parameters.

The convergence rate shows that the solution of the general problem is non-smooth, due to the presence of multiple cell contact (or 2 cells and the extracellular domain.) The single cell problem is instead smooth. To the best of our knowledge, there are no regularity results for the single cell problem, except for those provided in [25] on asymptotic solutions. For the one-cell problem (1) with smooth interface, but $\sigma_1 \neq \sigma_0$, the solution is probably regular. Intuitively, the interface problem with piecewise smooth coefficients and fixed transmembrane potential (that is, at the equilibrium) can be recast, via lifting [49], to a more classical interface problem already studied by Babuška [50] and Kellogg [51], who showed that the solution is at least H^2 on each subdomain.

Well-posedness results for the general EMI problem are found in [17,24], however we are not aware of regularity results for the general EMI problem (39). For two or more cells in contact, subdomains must be polygonal, which limits the regularity. The singularities introduced by the contact have been analyzed by Nicaise and Sändig [52]. These results should be taken in consideration in the development of higher order numerical schemes for the solution of the EMI problem.

We also show that the discretization parameters are not too restrictive, when compared to the more standard (homogenized) bidomain or monodomain model. A typical time step is 0.02 ms or lower for IMEX solvers [53]. In space, we observed here that a mesh resolution for the membrane of 10 µm is sufficiently accurate for the cell-by-cell model. On the other hand, for the standard bidomain the mesh size depends on the front thickness, in turn depending on tissue excitability and conductivity. An accepted value is 100 µm to 200 µm [43]. However, this is only true in the fiber direction and for healthy tissue, since in fibrotic tissue or in the cross-fiber direction the front thickness is

generally lower [44,54]. Finally, we observed here that propagation failure can occur in the EMI model, in contrast to the bidomain model. This aspect is very important in the study of pathological situations. It is important to remark that our formulation requires constant coefficients within each cell, but not on the membrane. The inclusion of more subdomains, e.g., different cell types or intracellular components, can be used to model heterogeneities. This approach is different from the standard (homogenized) bidomain system, where the effective conductivity coefficients must be non-constant in order to account for structural microscale heterogeneities.

This work paves the way in two directions. First, for designing another method where a more realistic cell-by-cell model is solved, i.e., where the linear algebraic condition on the gap junctions is replaced by a stiff nonlinear ordinary differential equation. Second, it provides the mathematical framework for solving the EMI model in three dimensions with a boundary integral formulation.

Declaration of competing interest

The authors declare the following financial interests/personal relationships which may be considered as potential competing interests: All authors reports financial support was provided by EuroHPC MICROCARD grant agreement No 955495.

Data availability

Code available here: .

Acknowledgments

We are very grateful to Michael Multerer for kindly sharing the initial BEM code and the fruitful discussion on the problem. We also thank the MICROCARD consortium for the suggestions for improving the manuscript.

Appendix. Poincaré–Steklov map on Ω_0

Here we briefly describe how to derive the Poincaré–Steklov operators P_0, P_0 on Ω_0 used in Eqs. (9) and (17), respectively.

Let $\Phi \in \{\Gamma_0, \Sigma\}$, we introduce the restricted trace operators

$$\begin{aligned} &\gamma^0_{t,\Phi} : H^1(\Omega_0) \to H^{1/2}(\Phi), \qquad \gamma^0_{t,\Phi} u_0(\boldsymbol{x}) = \lim_{\Omega_0 \ni \boldsymbol{y} \to \boldsymbol{x} \in \Phi} u_0(\boldsymbol{y}), \\ &\gamma^0_{n,\Phi} : H^1(\Omega_0) \to H^{-1/2}(\Phi), \qquad \gamma^0_{n,\Phi} u_0(\boldsymbol{x}) = \lim_{\Omega_0 \ni \boldsymbol{y} \to \boldsymbol{x} \in \Phi} \langle \nabla u_0(\boldsymbol{y}), \boldsymbol{n}_0 \rangle. \end{aligned} \tag{A.1}$$

From the Green's representation formula we have

$$\begin{aligned} u_0(\boldsymbol{x}) = &\int_{\Gamma_0} \gamma^0_{t,\boldsymbol{y}} G(\boldsymbol{x},\boldsymbol{y}) \gamma^0_{n,\Gamma_0} u_0(\boldsymbol{y}) \mathrm{d}s_{\boldsymbol{y}} + \int_{\Sigma} \gamma^0_{t,\boldsymbol{y}} G(\boldsymbol{x},\boldsymbol{y}) \gamma^0_{n,\Sigma} u_0(\boldsymbol{y}) \mathrm{d}s_{\boldsymbol{y}} \\ &- \int_{\Gamma_0} \gamma^0_{n,\boldsymbol{y}} G(\boldsymbol{x},\boldsymbol{y}) \gamma^0_{t,\Gamma_0} u_0(\boldsymbol{y}) \mathrm{d}s_{\boldsymbol{y}} - \int_{\Sigma} \gamma^0_{n,\boldsymbol{y}} G(\boldsymbol{x},\boldsymbol{y}) \gamma^0_{t,\Sigma} u_0(\boldsymbol{y}) \mathrm{d}s_{\boldsymbol{y}}, \quad \boldsymbol{x} \in \Omega_0. \end{aligned} \tag{A.2}$$

For $\Phi, \Psi \in \{\Gamma_0, \Sigma\}$, we define

$$\begin{aligned} &\mathcal{V}_0^{\Psi,\Phi} : H^{-1/2}(\Phi) \to H^{1/2}(\Psi), \qquad \mathcal{V}_0^{\Psi,\Phi} \rho(\boldsymbol{x}) = \int_{\Phi} \gamma^0_{0,\boldsymbol{y}} G(\boldsymbol{x},\boldsymbol{y}) \rho(\boldsymbol{y}) \mathrm{d}s_{\boldsymbol{y}}, \qquad \boldsymbol{x} \in \Psi, \\ &\mathcal{K}_0^{\Psi,\Phi} : H^{1/2}(\Phi) \to H^{1/2}(\Psi), \qquad \mathcal{K}_0^{\Psi,\Phi} \rho(\boldsymbol{x}) = \int_{\Phi} \gamma^0_{1,\boldsymbol{y}} G(\boldsymbol{x},\boldsymbol{y}) \rho(\boldsymbol{y}) \mathrm{d}s_{\boldsymbol{y}}, \qquad \boldsymbol{x} \in \Psi, \end{aligned} \tag{A.3}$$

applying the trace operators γ^0_{t,Γ_0} and $\gamma^0_{n,\Sigma}$ to Eq. (A.2) yields

$$\begin{aligned} \gamma^0_{t,\Gamma_0} u_0 &= \mathcal{V}_0^{\Gamma_0,\Gamma_0} \gamma^0_{n,\Gamma_0} u_0 + \mathcal{V}_0^{\Gamma_0,\Sigma} \gamma^0_{n,\Sigma} u_0 - (\mathcal{K}_0^{\Gamma_0,\Gamma_0} - \tfrac{1}{2} I) \gamma^0_{t,\Gamma_0} u_0 - \mathcal{K}_0^{\Gamma_0,\Sigma} \gamma^0_{t,\Sigma} u_0, \\ \gamma^0_{t,\Sigma} u_0 &= \mathcal{V}_0^{\Sigma,\Gamma_0} \gamma^0_{n,\Gamma_0} u_0 + \mathcal{V}_0^{\Sigma,\Sigma} \gamma^0_{n,\Sigma} u_0 - \mathcal{K}_0^{\Sigma,\Gamma_0} \gamma^0_{t,\Gamma_0} u_0 - (\mathcal{K}_0^{\Sigma,\Sigma} - \tfrac{1}{2} I) \gamma^0_{t,\Sigma} u_0, \end{aligned} \tag{A.4}$$

which, after manipulation and setting $\gamma^0_{n,\Sigma} u_0 = 0$ (cf. Eq. (39)(g)), result in

$$\begin{aligned} (\mathcal{K}_0^{\Gamma_0,\Gamma_0} + \tfrac{1}{2} I) \gamma^0_{t,\Gamma_0} u_0 &= \mathcal{V}_0^{\Gamma_0,\Gamma_0} \gamma^0_{n,\Gamma_0} u_0 - \mathcal{K}_0^{\Gamma_0,\Sigma} \gamma^0_{t,\Sigma} u_0, \\ (\mathcal{K}_0^{\Sigma,\Sigma} + \tfrac{1}{2} I) \gamma^0_{t,\Sigma} u_0 &= \mathcal{V}_0^{\Sigma,\Gamma_0} \gamma^0_{n,\Gamma_0} u_0 - \mathcal{K}_0^{\Sigma,\Gamma_0} \gamma^0_{t,\Gamma_0} u_0. \end{aligned} \tag{A.5}$$

Solving for $\gamma_{n,\Gamma_0} u_0, \gamma_{t,\Sigma} u_0$ with respect to $\gamma_{t,\Gamma_0} u_0$ yields the linear relation Eq. (9) (dropping Γ_0 from the notation).

We discretize $\Gamma_0 = \Gamma_1$ as in Section 2.2 (same collocation points) and place $\overline{M}$ collocation points $\overline{\boldsymbol{x}}_j$ on Σ. We compute a smooth parametrization $\gamma_\Sigma : [0,1) \to \mathbb{R}^d$ of Σ, $\gamma_\Sigma(s_j) = \overline{\boldsymbol{x}}_j$, by Fourier interpolation (as for Γ_0) and represent

$$\begin{aligned} &\gamma^0_{t,\Gamma_0} u_0(\gamma_{\Gamma_0}(t)) = \sum_{j=1}^{M} u^j_{0,\Gamma_0} L_j(t), \quad \gamma^0_{n,\Gamma_0} u_0(\gamma_{\Gamma_0}(t)) = \sum_{j=1}^{M} \tilde{u}^j_{0,\Gamma_0} L_j(t), \\ &\gamma^0_{t,\Sigma} u_0(\gamma_\Sigma(t)) = \sum_{j=1}^{\overline{M}} u^j_{0,\Sigma} \overline{L}_j(t), \end{aligned} \tag{A.6}$$

with $\overline{L}_j(s)$ the trigonometric Lagrange basis functions satisfying $\overline{L}_j(s_i) = \delta_{ij}$, $i,j = 1,\dots,\overline{M}$. Inserting Eq. (A.6) into Eq. (A.5) yields

$$\begin{aligned} (K_0^{\Gamma_0,\Gamma_0} + \tfrac{1}{2} I) \boldsymbol{u}_{0,\Gamma_0} &= V_0^{\Gamma_0,\Gamma_0} \tilde{\boldsymbol{u}}_{0,\Gamma_0} - K_0^{\Gamma_0,\Sigma} \boldsymbol{u}_{0,\Sigma}, \\ (K_0^{\Sigma,\Sigma} + \tfrac{1}{2} \overline{I}) \boldsymbol{u}_{0,\Sigma} &= V_0^{\Sigma,\Gamma_0} \tilde{\boldsymbol{u}}_{0,\Gamma_0} - K_0^{\Sigma,\Gamma_0} \boldsymbol{u}_{0,\Gamma_0}, \end{aligned} \tag{A.7}$$

with $(\boldsymbol{u}_{0,\Gamma_0})_j = u^j_{0,\Gamma_0}, (\tilde{\boldsymbol{u}}_{0,\Gamma_0})_j = \tilde{u}^j_{0,\Gamma_0}, (\boldsymbol{u}_{0,\Sigma})_j = u^j_{0,\Sigma}$ and

$$(K_0^{\Gamma_0,\Gamma_0})_{kj} = \mathcal{K}_0^{\Gamma_0,\Gamma_0}(L_j \circ \gamma_{\Gamma_0}^{-1})(\boldsymbol{x}_k), \quad (K_0^{\Sigma,\Gamma_0})_{kj} = \mathcal{K}_0^{\Sigma,\Gamma_0}(L_j \circ \gamma_{\Gamma_0}^{-1})(\overline{\boldsymbol{x}}_k), \tag{A.8}$$

$$(K_0^{\Sigma,\Sigma})_{kj} = \mathcal{K}_0^{\Sigma,\Sigma}(\overline{L}_j \circ \gamma_\Sigma^{-1})(\overline{\boldsymbol{x}}_k), \quad (K_0^{\Gamma_0,\Sigma})_{kj} = \mathcal{K}_0^{\Gamma_0,\Sigma}(\overline{L}_j \circ \gamma_\Sigma^{-1})(\boldsymbol{x}_k), \tag{A.9}$$

and similarly for $V_0^{\Sigma,\Gamma_0}, V_0^{\Gamma_0,\Gamma_0}$. Solving for $\tilde{\boldsymbol{u}}_{0,\Gamma_0}, \boldsymbol{u}_{0,\Sigma}$ with respect to $\boldsymbol{u}_{0,\Gamma_0}$ yields

$$\tilde{\boldsymbol{u}}_{0,\Gamma_0} = P_0 \boldsymbol{u}_{0,\Gamma_0}, \tag{A.10}$$

which is employed in Eqs. (17) and (18) (dropping Γ_0 from the notation).

References

[1] Kléber AG, Rudy Y. Basic mechanisms of cardiac impulse propagation and associated arrhythmias. Physiol Rev 2004;84(2):431–88.
[2] Neu J, Krassowska W. Homogenization of syncytial tissues. Crit Rev Biomed Eng 1993;21(2):137–99.
[3] Spach MS, Heidlage JF. The stochastic nature of cardiac propagation at a microscopic level: electrical description of myocardial architecture and its application to conduction. Circ Res 1995;76(3):366–80.
[4] Tveito A, Mardal K-A, Rognes ME. Modeling excitable tissue: the EMI framework. Springer Nature; 2021.
[5] Schotten U, Verheule S, Kirchhof P, Goette A. Pathophysiological mechanisms of atrial fibrillation: a translational appraisal. Physiol Rev 2011;91(1):265–325. http://dx.doi.org/10.1152/physrev.00031.2009.
[6] Stinstra J, Henriquez C, MacLeod R. Comparison of microscopic and bidomain models of anisotropic conduction. Comput Cardiol 2009;36:657–60.
[7] Stinstra J, MacLeod R, Henriquez C. Incorporating histology into a 3D microscopic computer model of myocardium to study propagation at a cellular level. Ann Biomed Eng 2010;38:1399–414.
[8] Stinstra J, Poelzing S, MacLeod R, Henriquez C. A model for estimating the anisotropy of the conduction velocity in cardiac tissue based on the tissue morphology. Comput Cardiol 2007;34:129–32.
[9] Stinstra JG, Hopenfeld B, MacLeod RS. On the passive cardiac conductivity. Ann Biomed Eng 2005;33:1743–51.
[10] Jæger KH, Edwards AG, Giles WR, Tveito A. Arrhythmogenic influence of mutations in a myocyte-based computational model of the pulmonary vein sleeve. Sci Rep 2022;12.
[11] Tveito A, Jæger KH, Kuchta M, Mardal KA, Rognes ME. A cell-based framework for numerical modeling of electrical conduction in cardiac tissue. Front Phys 2017;5.
[12] Daversin-Catty C, Richardson CN, Ellingsrud AJ, Rognes ME. Abstractions and automated algorithms for mixed domain finite element methods. ACM Trans Math Softw 2021;47(4):1–36.
[13] Hand PE, Griffith BE, Peskin CS. Deriving macroscopic myocardial conductivities by homogenization of microscopic models. Bull Math Biol 2009;71:1707–26.

[14] Bécue P-E, Caro F, Potse M, Coudière Y. Theoretical and numerical study of cardiac electrophysiology problems at the microscopic scale. In: SIAM conference on the life sciences (LS16). 2016, URL https://hal.inria.fr/hal-01405837, Poster.
[15] Bécue P-E, Potse M, Coudière Y. Microscopic simulation of the cardiac electrophysiology: A study of the influence of different gap junctions models. In: 2018 computing in cardiology conference (CinC), Vol. 45. IEEE; 2018, p. 1–4.
[16] Bécue P-E, Potse M, Coudière Y. A three-dimensional computational model of action potential propagation through a network of individual cells. In: 2017 computing in cardiology (CinC). 2017, p. 1–4. http://dx.doi.org/10.22489/CinC.2017.022-271.
[17] Bécue P-E. Modélisation et simulation de l'électrophysiologie cardiaque à l'échelle microscopique. (Ph.D. thesis), Université de Bordeaux; 2018, URL https://theses.hal.science/tel-02019648.
[18] Foster KR, Sowers AE. Dielectrophoretic forces and potentials induced on pairs of cells in an electric field. Biophys J 1995;69:777–84.
[19] Hogues H, Leon LJ, Roberge FA. A model study of electric field interactions between cardiac myocytes. IEEE Trans Biomed Eng 1992;39:1232–43.
[20] Leon LJ, Roberge FA. A model study of extracellular stimulation of cardiac cells. IEEE Trans Biomed Eng 1993;40:1307–19.
[21] Vigmond EJ, Velazquez JLP, Valiante TA, Bardakjian BL, Carlen PL. Mechanisms of electrical coupling between pyramidal cells. J Neurophysiol 1997;78(6):3107–16.
[22] Henríquez F, Jerez-Hanckes C. Multiple traces formulation and semi-implicit scheme for modelling biological cells under electrical stimulation. ESAIM Math Model Numer Anal 2018;52:659–702.
[23] Henríquez F, Jerez-Hanckes C, Altermatt F. Boundary integral formulation and semi-implicit scheme coupling for modeling cells under electrical stimulation. Numer Math 2017;136:101–45.
[24] Colli Franzone P, Savaré G. Degenerate evolution systems modeling the cardiac electric field at micro-and macroscopic level. Evol Equations Semigroups Funct Anal: Mem Brunello Terreni 2002;49–78.
[25] Matano H, Mori Y. Global existence and uniqueness of a three-dimensional model of cellular electrophysiology. Discrete Contin Dyn Syst 2011;29(4):1573–636.
[26] Colli Franzone P, Pavarino LF, Taccardi B. Simulating patterns of excitation, repolarization and action potential duration with cardiac bidomain and monodomain models. Math Biosci 2005;197:35–66. http://dx.doi.org/10.1016/j.mbs.2005.04.003.
[27] Sauter SA, Schwab C. Boundary element methods. Springer; 2011.
[28] Kress R. Linear integral equations. Springer; 1989.
[29] Steinbach O. Numerical approximation methods for elliptic boundary value problems: finite and boundary elements. Springer; 2007.
[30] Gander L, Krause R, Multerer M, Pezzuto S. Space–time shape uncertainties in the forward and inverse problem of electrocardiography. Int J Numer Methods Biomed Eng 2021;37:1–23. http://dx.doi.org/10.1002/cnm.3522.
[31] Langer U, Steinbach O. Boundary element tearing and interconnecting methods. Computing 2003;71:205–28.
[32] Benzi M, Golub GH, Liesen J. Numerical solution of saddle point problems. Acta Numer 2005;14:1–137.
[33] Jæger KH, Hustad KG, Cai X, Tveito A. Efficient numerical solution of the EMI model representing the extracellular space (E), cell membrane (M) and intracellular space (I) of a collection of cardiac cells. Front Phys 2021;8:579461.
[34] Abdulle A, Grote MJ, Rosilho de Souza G. Explicit stabilized multirate method for stiff differential equations. Math Comp 2022;91:2681–714.
[35] Rosilho De Souza G. mRKC: A multirate Runge–Kutta–Chebyshev code. 2022, URL https://github.com/grosilho/mRKC.
[36] der Houwen PJV, Sommeijer BP. On the internal stability of explicit, *m*-stage Runge–Kutta methods for large *m*-values. Z Angew Math Mech 1980;60:479–85.
[37] Rosilho de Souza G. BEMI: A C++ implementation of the BEM method for solving the EMI model in 2D. 2023, URL https://github.com/grosilho/BEMI.
[38] Guennebaud G, Jacob B, et al. Eigen v3. 2010, http://eigen.tuxfamily.org.
[39] Cuellar AA, Lloyd CM, Nielsen PF, Bullivant DP, Nickerson DP, Hunter PJ. An overview of cellml 1.1, a biological model description language. Simulation 2003;79:740–7.
[40] Clerx M, Collins P, de Lange E, Volders PG. Myokit: A simple interface to cardiac cellular electrophysiology. Prog Biophys Mol Biol 2016;120:100–14.
[41] Courtemanche M, Ramirez RJ, Nattel S. Ionic mechanisms underlying human atrial action potential properties: insights from a mathematical model. Am J Physiol-Heart Circul Physiol 1998;275:H301–21.
[42] Clayton RH, Bernus O, Cherry EM, Dierckx H, Fenton FH, Mirabella L, Panfilov AV, Sachse FB, Seemann G, Zhang H. Models of cardiac tissue electrophysiology: Progress, challenges and open questions. Prog Biophys Mol Biol 2011;104:22–48.
[43] Niederer SA, Kerfoot E, Benson AP, Bernabeu MO, Bernus O, Bradley C, Cherry EM, Clayton R, Fenton FH, Garny A, Heidenreich E, Land S, Maleckar M, Pathmanathan P, Plank G, Rodríguez JF, Roy I, Sachse FB, Seemann G, Skavhaug O, Smith NP. Verification of cardiac tissue electrophysiology simulators using an N-version benchmark. Phil Trans R Soc A 2011;369:4331–51.
[44] Pezzuto S, Hake J, Sundnes J. Space-discretization error analysis and stabilization schemes for conduction velocity in cardiac electrophysiology. Int J Numer Methods Biomed Eng 2016;32:e02762, Referenze 12, 13, 14.
[45] Nowak MB, Veeraraghavan R, Poelzing S, Weinberg SH. Cellular size, gap junctions, and sodium channel properties govern developmental changes in cardiac conduction. Front. Physiol. 2021;12:731025.
[46] Rosilho de Souza G, Pezzuto S, Krause R. Effect of gap junction distribution, size, and shape on the conduction velocity in a cell-by-cell model for electrophysiology. In: Bernard O, Clarysse P, Duchateau N, Ohayon J, Viallon M, editors. Functional imaging and modeling of the heart. Lecture notes in computer science, Vol. 13958, Cham: Springer; 2023, p. 117–26. http://dx.doi.org/10.1007/978-3-031-35302-412.
[47] Jæger KH, Edwards AG, McCulloch A, Tveito A. Properties of cardiac conduction in a cell-based computational model. PLoS Comput Biol 2019;15(5):e1007042.
[48] Ivanovic E, Kucera JP. Localization of na+ channel clusters in narrowed perinexi of gap junctions enhances cardiac impulse transmission via ephaptic coupling: a model study. J Physiol 2021;599(21):4779–811.
[49] Chen Z, Zou J. Finite element methods and their convergence for elliptic and parabolic interface problems. Numer Math 1998;79(2):175–202.
[50] Babuška I. The finite element method for elliptic equations with discontinuous coefficients. Computing 1970;5(3):207–13.
[51] Kellogg BR. On the Poisson equation with intersecting interfaces. Appl Anal 1974;4(2):101–29.
[52] Nicaise S, Sändig A-M. General interface problems—I. Math Methods Appl Sci 1994;17(6):395–429.
[53] Krause D, Potse M, Dickopf T, Krause R, Auricchio A, Prinzen FW. Hybrid parallelization of a large-scale heart model. In: Keller R, Kramer D, Weiss J-P, editors. Facing the multicore-challenge ii. Lecture notes in computer science, Vol. 7174, Berlin: Springer; 2012, p. 120–32. http://dx.doi.org/10.1007/978-3-642-30397-5_11.
[54] Ruiz Herrera C, Grandits T, Plank G, Perdikaris P, Sahli Costabal F, Pezzuto S. Physics-informed neural networks to learn cardiac fiber orientation from multiple electroanatomical maps. Eng Comput 2022;38(5):3957–73.